A HYBRID NAVIER-STOKES/VORTEX PARTICLE WAKE METHODOLOGY FOR MODELING HELICOPTER ROTORS IN FORWARD FLIGHT AND MANEUVERS

A Dissertation
Presented to
The Academic Faculty

by

Luke Sterling Battey

In Partial Fulfillment
of the Requirements for the Degree
Master of Science in the
School of Aerospace Engineering

Georgia Institute of Technology
May 2018

A HYBRID NAVIER-STOKES/VORTEX PARTICLE WAKE METHODOLOGY FOR MODELING HELICOPTER ROTORS IN FORWARD FLIGHT AND MANEUVERS

Approved by:

Dr. Lakshmi N. Sankar, Advisor
School of Aerospace Engineering
Georgia Institute of Technology

Dr. Daniel Schrage
School of Aerospace Engineering
Georgia Institute of Technology

Dr. J.V.R. Prasad
School of Aerospace Engineering
Georgia Institute of Technology

Dr. Stephen M. Ruffin
School of Aerospace Engineering
Georgia Institute of Technology

Date Approved: 9th April, 2

TABLE OF CONTENTS

LIST OF TABLES

LIST OF FIGURES

CHAPTER 1

INTRODUCTION

Rotary wing aircraft experience some of the most unique and complicated physical phenomena known to the aerospace community. At higher advance ratios, the inherently unsteady three-dimensional flow field produces compressibility effects on the advancing blade and dynamic stall on the retreating blade. The rotor blades also experience varying degrees of blade vortex interactions from neighboring blades and aeroelastic effects. In steady forward flight, the several effects must be managed properly if it is desired to provide a comfortable flying experience with an acceptable vehicle figure of merit. For maneuvering flight, the aeroelastic effects are exacerbated and high stresses are endured by crucial structural components of the rotor and hub, governing the durability that must be achieved by the design. To operate in these flight conditions, and hovering or climbing, the final design must come to fruition considering the perceived influence of the many potential physical phenomena.

1.1 Motivation

The accurate prediction of the aerodynamic effects and resulting loads on a rotorcraft's blades remains a paramount task in the aerospace industry. This is due to the implications it could have on the design process of getting a rotorcraft from a conceptual state to a physical and functional one. Rotorcraft design consists of an iterative process where aspects of the system are constantly being evaluated and refined. The most obvious way of evaluating different components is through experimental testing. However, this would be prohibitively expensive in determining the efficacy of every design configuration, making preliminary analysis tools a required part of the design process. Physics-based models are often considered superior compared to generalized empirical models due to the ability of manipulating any specific design

parameter. How effective in progressing a design these models are greatly depends on their accuracy and ease of use. Computational fluid dynamics (CFD) codes are perhaps one of the most depended-on tools when it comes to rotorcraft design. The use of CFD in predicting the aerodynamic loads on rotorcraft greatly enhances the engineer's understanding of certain design requirements early in the process, saving considerable time and cost. As such, CFD tools have undoubtedly become a staple in the rotorcraft community.

1.2 State of the Art

The overall accuracy of the rotorcraft CFD codes that are considered the best has dramatically improved over the last few decades. This can be largely attributed to the rapid increase in computing capability and affordability. With increasingly powerful computers that are practically affordable to use on a simulation, the CFD solvers can conduct more and more comprehensive modeling for a given situation. In other words, fewer assumptions can be made that lower the fidelity of a solution, because it is often less of a concern to just spend more computational resources. Perhaps the most evident example of utilizing high computational power is using fine meshes which fully resolve and capture the effects of a rotor's wake, such as the extensively used OVERFLOW [1,2]. Users can employ grids with hundreds of millions of points to capture any potential flow physics that may occur. Thus, with the use of massive high-end supercomputers, the current state of the art rotorcraft codes can determine the blades' aerodynamic loads so accurately that only a 0.2% error in the figure of merit is obtained [3]. This of course doesn't leave much room for improvement in terms of accuracy alone. Other rotorcraft CFD codes use a chimera grid approach which contains near body grids around each rotor blade and a small rectangular grid used to resolve the near wake. A hybrid wake approach, as the current work utilizes, consists of only one near-body grid to resolve the flow field around a

single blade. The far-wake and wake of other blades are all modeled in a Lagrangian manner, making hybrid wake codes the least computationally intensive variety of CFD solvers.

1.3 What is Missing

While the most comprehensive rotorcraft CFD codes have a nearly unbeatable accuracy, they are inferior in terms of computational cost. To obtain the most accurate possible solution from the current state of the art code can take weeks of runtime on a supercomputer with thousands of processors and require many terabytes of disk space. Unfortunately, many researchers and designers wouldn't have this magnitude of computational resources readily available to them. Because of this, lower fidelity codes are often used where it is considered acceptable that even if the results aren't perfect, they can still be meaningful. The code studied here, GT-Hybrid, which was introduced by Sankar *et al*. [4] and improved upon through many iterations [5,6], fits into this description. While this and other hybrid solvers have shown to efficiently provide useful results, there is still thought to be room for improvement in both fidelity and computational time. Thus, it is desired to implement a different methodology of modeling the wake to GT-Hybrid that is thought to emulate reality more closely. As such, the addition of this wake methodology, which is described in detail in a following section, has potential to improve the accuracy of the codes' solution, but inadequate research for the comparison of methods has been done thus far. Furthermore, the efficacy of using this alternative wake method to model unsteady maneuvering flight has yet to be determined. The purpose of this work is to help fill the voids that previous research has left by exploring potential differences between the two Lagrangian wake methods that can be used in a hybrid wake rotorcraft CFD code, such as in the computational time, resulting accuracy, or other unique qualities.

CHAPTER 2

NUMERICAL FORMULATION

In this chapter, several underlying concepts are discussed that together are used to achieve a final solution for a given simulation. First, details of the hybrid CFD methodology are explained, followed by the CSD methodology and how the iterative coupling is performed. For brevity, this is not a comprehensive description, but key aspects are covered with references to more detailed information being available throughout. Next, the formulation for the recently implemented vortex particle method is described in detail. Lastly, some numerical studies concerning the wake are provided that aided in selecting certain options that were used during the implementation.

2.1 CFD Methodology

GT-Hybrid employs a hybrid wake methodology to obtain the numerical solution of the blade loads and other properties. This means that the flowfield is only resolved within a small gridded domain surrounding a single rotor blade. Within this grid, the discretized Navier-Stokes solutions are solved using a time-accurate flux-limited MUSCL scheme with 3rd order spatial and 1st order temporal accuracy [7, 8]. The solver is also capable of 5th order spatial and 2nd order temporal accuracy. However, they have been demonstrated to be far more computationally intensive without significant accuracy improvements [9], and thus are not used in this work. The solver contains three optional turbulence models along with a fully laminar assumption. The turbulence model used here was the Spalart-Allmaras Detached Eddy Simulation (SA-DES) model [10] due to its previously demonstrated superiority in these cases [9]. Minimizing the domain where the solution is resolved provides an efficient means of calculating the aerodynamic loads on a rotor blade. To do this accurately, though, effects beyond this small

domain must be accounted for. This is done by modeling the wake of each rotor blade with a grid-free field of vorticity elements. The wake and other key details of the solver are discussed in the following subsections. More comprehensive documentation on the theory as well as using GT-Hybrid and the specific user-controlled parameters can be found in the user's manual [11].

2.1.1 Computational Grid

To computationally discretize a region near a rotor blade, GT-Hybrid uses a C-H grid topology, which has a single block that essentially wraps around the airfoil surface, continuing past the trailing edge. This type of grid has a well-defined, simple structure to it which allows for relatively fast grid generation with automated programs.
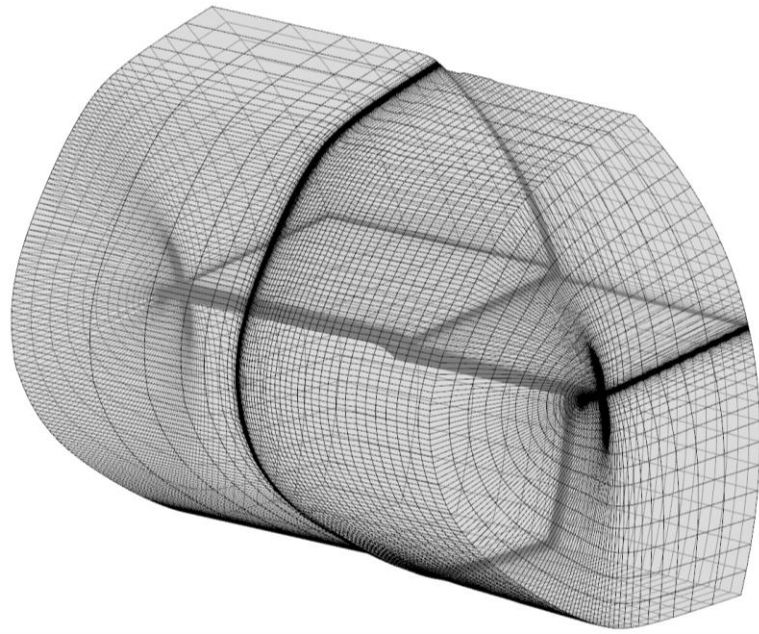
Figure 1: UH-60A Rotor Blade C-H Grid

The C-H grid used in this work for the UH-60A is shown below in Figure 1, having i-, j-, and k-max values of 131, 65, and 45, which correspond to the chordwise, spanwise, and normal directions, respectively. This results in a blade surface of 91 chordwise points and 50 spanwise points. The small 383,175-point grid offers fast computation, especially when compared to

solvers that fully resolve the wake, having tens or even hundreds of millions of points. The UH-60A grid has been carefully constructed [12] and used in a grid resolution study with three grids with i, j, k of 131x65x45, 263x65x90, and 263x128x90 points. It was observed that the most coarse grid used here gave the best compromise between accuracy and computational time for both steady and maneuvering flight [13].

The grid boundary is located about nine chord lengths away from the blade in the normal direction and about a radius away in the spanwise. Clustering is done along the blade leading and trailing edges, as well as near the blade tip, and in the normal direction away from the blade surface to adequately capture the regions with high pressure gradients.

Throughout the azimuthal range, pitching, flapping, and lead-lag motions are prescribed by rotating the entire grid in one of the three directions according to a so-called blade-motions file, which is an input to the code. This file can be manually entered by the user for a rigid blade simulation or created through CSD/CFD coupling with a structural dynamics code, explained more in section 2.2. For non-rigid blades, the blade-motions file can also include structural deformations due to elasticity. These motions are enforced by deforming the grid, a process conducted within GT-Hybrid as it runs.

2.1.2 Boundary Conditions

On the blade surface, being a subarea of the k=1 surface, viscous no-slip and adiabatic boundary conditions are used. The rest of the k=1 surface beyond the blade has points which can all be matched to corresponding points that share the same location, where interface (or coupled) boundary conditions are applied. At the exterior boundary, non-reflecting inflow/outflow boundary conditions are applied. The velocity vectors on the exterior grid points are the vector sums of the freestream velocity (caused by forward flight or maneuvering), the velocity caused

by azimuthal grid rotation (Ωr), and the induced velocity from the wake and bound vorticity generated by all blades. This induced velocity will be discussed later.

2.1.3 Wake model

The wake model traditionally used in GT-Hybrid is primarily based on Prandtl's lifting-line theory, Kelvin's theorem, and the Biot-Savart law [14]. The lifting-line theory represents the rotor blade as a line in the spanwise direction at quarter chord. From this line on each of the blades, the wake geometry and vorticity strengths are initialized as a perfectly helical structure with strong trailing tip vortices using an analytical model [15]. The wake consists of a lattice of tip-to-tail Biot-Savart vectors being in the azimuthal direction for trailing vortices and the spanwise for shed vortices. The number of Biot-Savart vectors (filaments) depends on how many radial stations the vortices are generated from, how often new vortices are created, and how many revolutions the wake is modeled as; all inputs from the user. A visual depiction of the wake model for a single blade is shown in Figure 2:
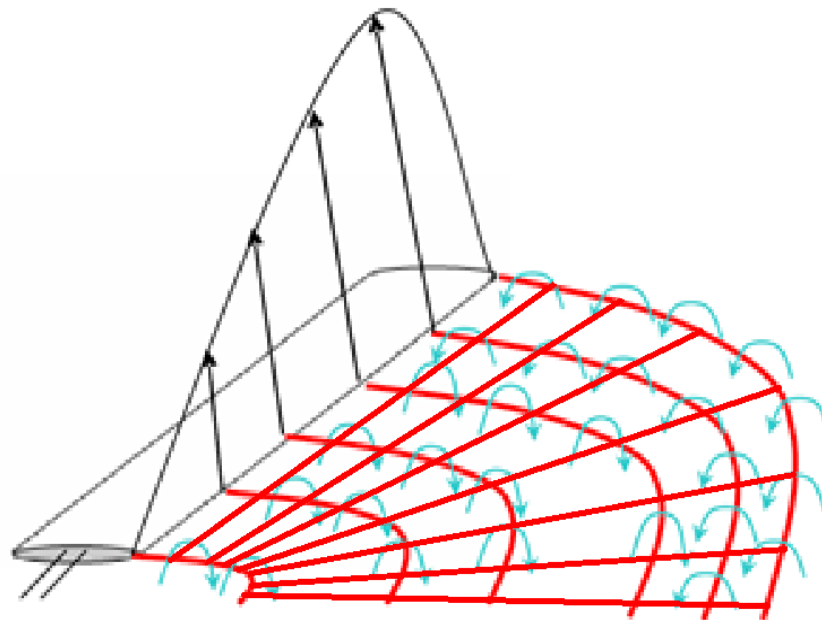
Figure 2: Wake Method Visualization

The strength of the trailing vortices (the vectors generated normal to the span) is a function of the spanwise change in bound vorticity, while the strength of the shed vortices (vectors in spanwise direction) is temporal change, both of which are correlated to changes in aerodynamic lift. As the blades rotate, the lift distribution is updated from the Navier-Stokes solution and new filaments are produced while the oldest filaments are deleted, enforcing the user-set constant wake size. It is prescribed that the lift distribution varies periodically, which allows for only solving on one blade even though there are several blades' worth of trailers. This is known to be an assumption, however, and could result in some error [16], but is accepted as the time savings are thought to be more significant. Using the Biot-Savart law on every wake filament is done to find the wake-induced velocity at any desired point. The straight vectors allow for following equation to be used to find the induced velocity from one filament:

$$\vec{V}_{induced} = \sum_{i=1}^{N} \left(\frac{\Gamma}{4\pi} \vec{r}_1 \times \vec{r}_2 \frac{|r_1 + r_2|\left(1 - \frac{\vec{r}_1 \cdot \vec{r}_2}{|r_1 r_2|}\right)}{|r_1 r_2|^2 - (\vec{r}_1 \cdot \vec{r}_2)^2 + r_c^2(r_1^2 + r_2^2 - 2\vec{r}_1 \cdot \vec{r}_2)} \right)_i \tag{1}$$

where Γ is the vorticity strength and $\vec{r}_1$ and $\vec{r}_2$ are vectors from the point in question to the tip and tail of a Biot-Savart vector, respectively. r_c is a scalar called the core radius, with the implementation here representing the Vatistas core model [17] to more accurately model each vortex so it has a finite and more physical induced velocity distribution. A core radius growth model existing in GT-Hybrid was introduced by Bhagwat and Leishman [18], and effectively models weakening of vortices due to viscous effects.

The induced velocity is used in two ways. First, to convect the wake by moving every wake filament by the induced velocity and freestream velocity at its location multiplied by the wake's time step. Second, to solve a velocity component of the grid's boundary condition, as mentioned above. It should be noted that the wake near the gridded blade is inherently captured

within the Navier-Stokes domain. To not double account for this vorticity, the induced velocity from filaments generated by this blade that are located inside the grid's surface is omitted from the boundary condition calculations, but still used to convect the wake.

2.2 CSD and Coupling

In accurately predicting the aerodynamics loads on a rotorcraft's blades, CFD alone is often not sufficient. One issue is that researchers and designers will often not know the collective and cyclic pitch inputs that result in a certain flight condition (thrust and hub moments), rather these crucial inputs to a CFD solver must be found beforehand. Even if pitching information is given from a previous flight test, there is no guarantee that the resulting aerodynamic loads will provide the correct thrust or hub moments due to imperfect modeling. Furthermore, the CFD alone provides no information about deformations due to blade elasticity, flapping, or lead-lag angles, motions that could significantly change the resulting aerodynamic loads. To combat these issues, the blade motions and trim settings need to be solved for externally.

2.2.1 CSD Methodology

The computational structural dynamics (CSD) methodology utilized here is provided by DYMORE 2, developed by Bauchau *et al.* [19] at the Georgia Institute of Technology. This code employs geometrically exact finite element analysis to numerically solve for component deflections without making assumptions. Many components of the rotor can be modeled with a multibody dynamics approach. For the UH-60A model, this includes the flexible blades, all hinges for full blade articulation, pitch-links, swash plate, linearly modeled dampers, and more. A visualization of some component modeling capabilities is provided in Figure 3:
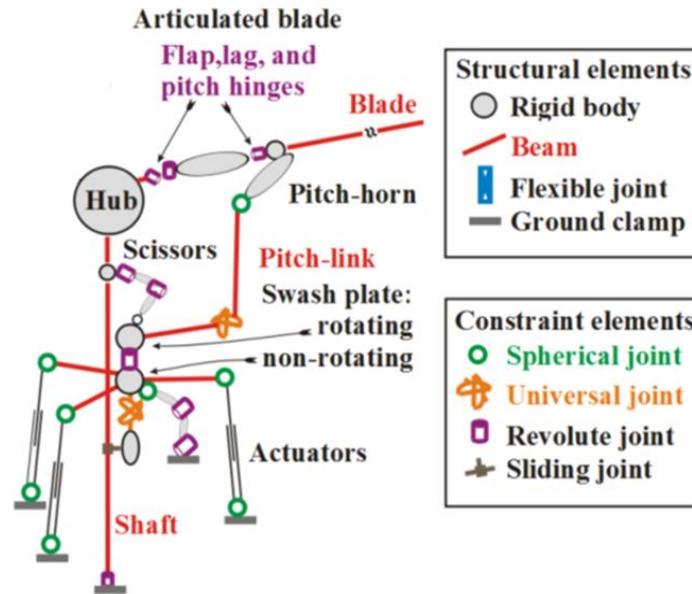
Figure 3: DYMORE 2 Model

Forces, moments, and deflections are then calculated on the many components as a function of azimuth for structural loading analysis and comparison with experimental data.

DYMORE 2 is not only a CSD code, however, but belongs to a class of solvers called rotorcraft comprehensive codes. This means it can perform complete trimmed aeroelastic analysis with a stand-alone run. This is accomplished with a built-in lifting line aerodynamics solver that uses a 2-D lookup airfoil table and a non-linear inflow model. Also available and used in this work is an autopilot feature, where the user can set thrust and hub moment targets for the solver to aim for. While the aerodynamics model is a vital asset here, it is well known that the accuracy of lifting line methods alone pale in comparison to that of CFD. As such, the aerodynamic forces from CFD computations can be used within DYMORE's model to increase accuracy, as is done here. This concept is built upon with coupling, described in the next section.

Several other modern comprehensive rotorcraft codes have been created and studied in literature, such as CAMRAD II [20], RCAS [21], and UMARC2 [22]. However, their variability is limited; it has been observed that using a certain one doesn't have a tremendous impact on the

10

final solutions when compared to others, because the CFD tends to drive the accuracy [23]. More specifically, GT-Hybrid has been used in conjunction with CAMRAD II and DYMORE [24] previously and showed the similar trend of minor differences between the rotorcraft comprehensive codes.

2.2.2 Coupling Methodology

Briefly mentioned in 2.2.1 was using CFD solvers in conjunction with CSD or rotorcraft comprehensive codes. This is generally done by employing either a tight or loose coupling method, which both allow giving accurate aerodynamic loads to the CSD code as well as structural and control information to the CFD code. Tight coupling is performed by simultaneously solving structural dynamics and fluid dynamics equations, then transferring information at every time step. The loose coupling approach transfers information periodically between solvers, here information from an entire rotor revolution is transferred at once. In theory, tight coupling is a more rigorous method, however, it complicates the numerical method and achieving trim is difficult. Furthermore, it has been shown that for high speed flight as studied here, tight coupling requires 2.5x the computational time as loose coupling but provides very similar solutions [25]. As such, the loose coupling methodology is adopted for this work with a delta-trim formulation [26]. In this method, shown schematically in Figure 4, the aerodynamic loads are first calculated with only DYMORE largely to conduct the trim.
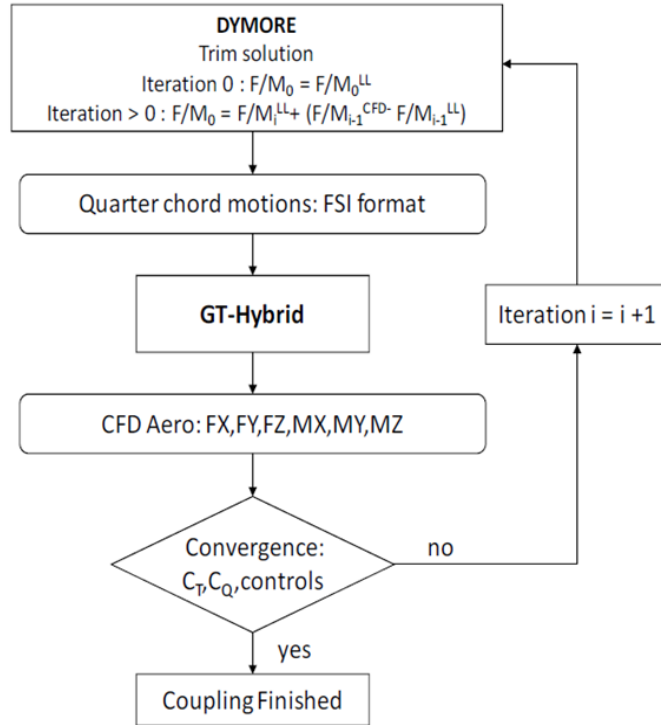
Figure 4: Delta-trim Loose Coupling

The pitch controls are then fed into GT-Hybrid, which better approximates the airloads and used them to increment the airloads in a following DYMORE run, yielding new trim and elasticity results. Iterations are done until thrust and hub moment converge. In this work, instead of checking convergence, 15 iterations are conducted which has been demonstrated to be more than enough [9].

2.3 Vortex Particle Methodology

The vortex particle method is an alternative approach to modeling vorticity that can also be applied to modeling rotor wakes without the use of a grid. Researchers have previously implemented vortex particle methods in different applications and achieved results that demonstrated its feasibility in rotorcraft aerodynamics [27]. It has even been observed that good agreements are seen with a lattice method [28], which has been traditionally used in GT-Hybrid.

Explained here are the details of the vortex particle method and how it is implemented into GT-Hybrid in place of the traditionally used wake model.

2.3.1 Model Uniqueness

Many of the traits of the vortex lattice method are shared with the author's implementation of the vortex particle method in GT-Hybrid. They both use the Prandtl lifting line theory to produce periodic vorticity elements to convect and impose velocity on the rotating C-H grid. Furthermore, they both begin with perfectly helical wakes that evolve as the solution progresses. The fundamental difference between the two models, however, is that instead of using vorticity trailers comprised of many tip-to-tail Biot-Savart vectors, the vortex particle method models the wake as many independent points, each with their own vector-valued vorticity. This takes away the non-physical stipulation of requiring each vortex vector to be connected. This also allows the use of less computationally intensive equations to solve for each element's induced velocity, thus decreasing the computation time, in theory. Another added benefit of this method is how efficiently shed wake can be modeled. With the lattice method, the shed wake vectors can't simply be vectorially added to the trailing wake, because they are in different directions and couldn't be tip-to-tail if added. The independent particles of the vortex particle method, however, do allow vector addition, making the induced velocity twice as fast with shed wake, if all other aspects were equal. This also means the vortex particle method uses less random-access memory, making it more scalable if desired.

Finding the vortex particle wake-induced velocity at any given point is done in an analogous manner to the Biot-Savart law. The two methods' vorticity vectors both follow the right-hand rule, meaning the direction of induced velocity is normal to the vorticity and a cross

13

(2)

product must be calculated for every element. The general function used to find the induced velocity caused by every particle at a certain point is as follows:

$$\vec{V}_{induced} = \sum_{i=1}^{N} K(|\vec{r_i}|) * (\vec{\alpha_i} \times \vec{r_i})$$

where $\vec{r_i}$ is a distance vector from the vortex particle to the point where the induced velocity is being determined and $\vec{\alpha_i}$ is a vorticity vector of a particle. $K(|\vec{r_i}|)$ is called the Biot-Savart kernel which is a scalar-valued function typically dependent on the magnitude of the distance vector and potentially other parameters. The kernel is not a specified function that is set in stone, rather the person implementing a vortex particle method has the freedom to either choose from a kernel developed previously by another researcher, or develop one themselves. Included in the kernel could be wide variety of modeling parameters, like a core radius growth model or something else to model other higher-order effects. Ultimately, the kernel is what controls the accuracy of the induced velocity calculation and the computation time required to solve for it. Because the kernel must be solved for at every vortex element at every induced velocity location for every time step, it is by far the largest contributor to the model's entire required computation time, potentially having large implications on it for a slight change to its complexity. As such, the specific kernel used is a key component of the vortex particle method that requires careful consideration and/or testing.

2.3.2 Biot-Savart Kernels

Two different kernels will be explained in detail in this section: First, one presented by Chengjian He and Jinggen Zhao [27], but slightly modified to include the core radius model, then another that is introduced by the author.

Calculating the He and Zhao kernel begins with defining a non-dimensional distance

parameter, ρ, which is given as:

$$\rho = \frac{|\vec{r}_i| + r_{c,i}}{\sigma} \tag{3}$$

where $\vec{r}_i$ is the same as in Eq. 2 and $r_{c,i}$ is a certain particle's core radius, as calculated by the

existing core radius growth model in GT-hybrid. σ is the product of two user-defined

parameters: C_σ, the particle overlapping parameter and h_{res}, the minimum flowfield resolution. It

is reported that a particle overlapping parameter of at least 1.0 is required for solution

convergence. Next, ρ is used to find the Gaussian distribution function, defined as:

$$\xi(\rho) = \frac{1}{(2\pi)^{3/2}} e^{-\rho^2/2} \tag{4}$$

Green's function also must be determined, which is found as:

$$G(\rho) = \frac{1}{4\pi\rho} \operatorname{erf}\left(\frac{\rho}{\sqrt{2}}\right) \tag{5}$$

where $\operatorname{erf}\left(\rho/\sqrt{2}\right)$ is the commonly known Gauss error function evaluated for $\rho/\sqrt{2}$. Finally, the

Biot-Savart kernel to be used in Eq. 2 is calculated as:

$$K(\rho) = \frac{|G(\rho) - \xi(\rho)|}{\sigma^3 \rho^2} \tag{6}$$

This kernel was demonstrated by He and Zhao to be able to provide accurate wake results for a

rotor in hover and forward flight. These results were shown to not be sensitive to the modeling

parameters, C_σ and h_{res}, provided that $C_\sigma \geq 1$.

The next Biot-Savart kernel is very simple compared to that of He and Zhao, and has

some interesting qualities associated with it. The value of this kernel is found again using $\vec{r}_i$ and

$r_{c,i}$ with no other modeling parameters, and is calculated as:

$$K\left(|\vec{r}_i| + r_{c,i}\right) = \frac{1}{4\pi\left(|\vec{r}_i| + r_{c,i}\right)^3} \tag{7}$$

It is noticed how much easier to calculate this kernel is than the previous one, as it

replaces Eqs. 3 through 6 and doesn't require the exponential and error functions, which are

typically intrinsic in Fortran and other coding languages, but computationally costly.

The two kernels are initially compared by fixing C_σ at 1.0 while varying the h_{res}

parameter in the He and Zhao kernel and comparing it to Eq. 7, which is done below in Figure 5:
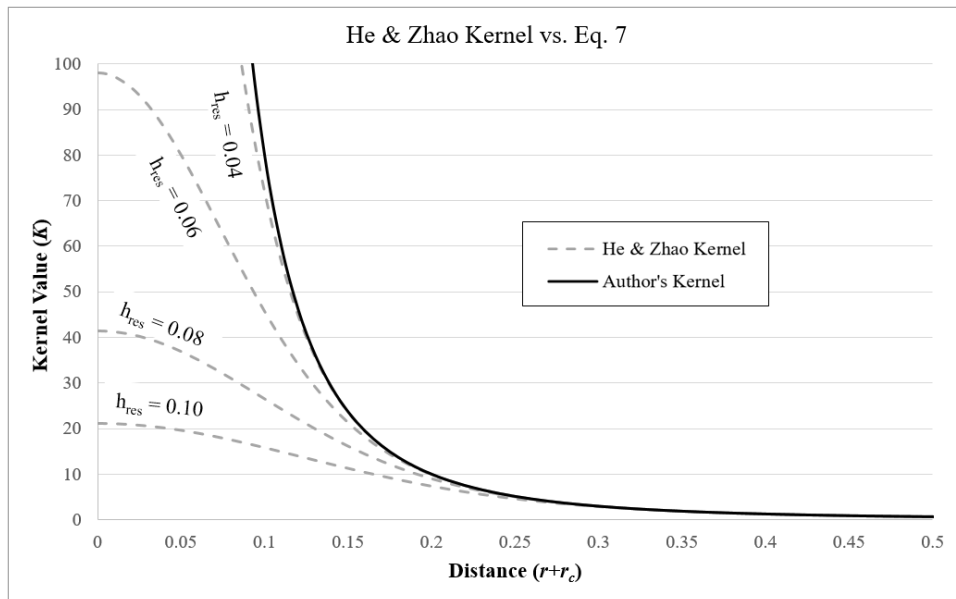
Figure 5: Kernel Comparisons

Here the physical input to the kernel, being the distance radius plus the core radius, is

plotted against the kernel's value. It is noticed that as the h_{res} parameter decreases, the He and

Zhao kernel quickly approaches the value from Eq. 7. This could also be shown mathematically

by taking the limit as $h_{res} \to 0$, which does in fact yield Eq. 7. Furthermore, all kernels begin to

coalesce above inputs of about 0.25. These qualities give promise to using this new kernel.

2.3.3 Particle Generation

Two different cases of generating the vortex particles are discussed here: the particles that produce the perfectly helical initial wake, and the particles that are generated with the actual CFD-resulting blade loads. First, the initial particle wake is prescribed by using what the traditional lattice wake would have been, with the particles placed at the mid-points of each filament. The vorticity vector then begins at that particle location and has the same direction as the other filament. Finally, the magnitude of the vorticity vector is equal to the gamma value for a filament multiplied by the filament's length. The initial lattice wake is not used for any induced velocity calculations, of course, but just offers a means of initializing the particle wake.

2.3.4 Wake Particle Resolution

Before the vortex particle method was implemented into GT-Hybrid, a sensitivity study was conducted to see how many particles were required to represent a wake and give similar accuracy to an equivalent lattice wake. To check this with a simple scenario, a straight-line vortex is constructed with a single Biot-Savart vector, representing one filament in a lattice wake. The vorticity strength, Γ, and vector length were chosen to be 1 to effectively non-dimensionalize the problem. For comparison, the line vortex is also constructed with 1 and 2 vortex particles with equivalent vorticity, and the resulting induced velocities are evaluated at different distances, as shown in Figure 6:
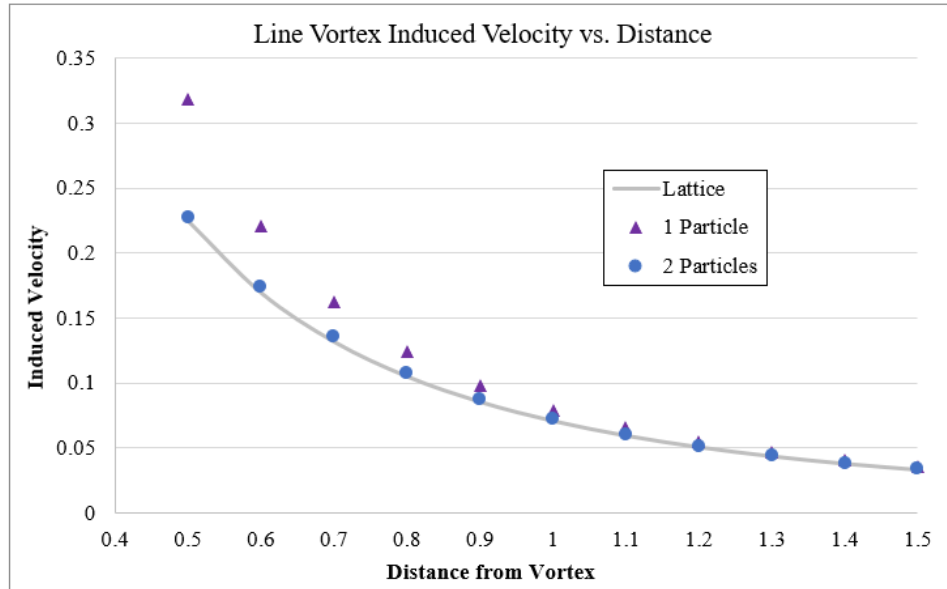
Figure 6: Particle Resolution Comparisons

It is observed that at smaller distances from the vortex, the single particle representation significantly overpredicts the induced velocity, while the two-particle version is very close to the lattice wake. At farther distances beyond about 1, however, all methods begin coalescing. These results indicate that the two-particle representation would be best to use, unless the induced velocity locations are typically at least one vector length away from each vortex vector.

To further study the particle resolution, the initial wake's induced velocity distribution on the surface of the computational grid was determined for three different wake representations: the lattice wake for the control, then two different particle wakes that used one and two vortex particles per lattice element to represent the wake, with results in Figure 7:
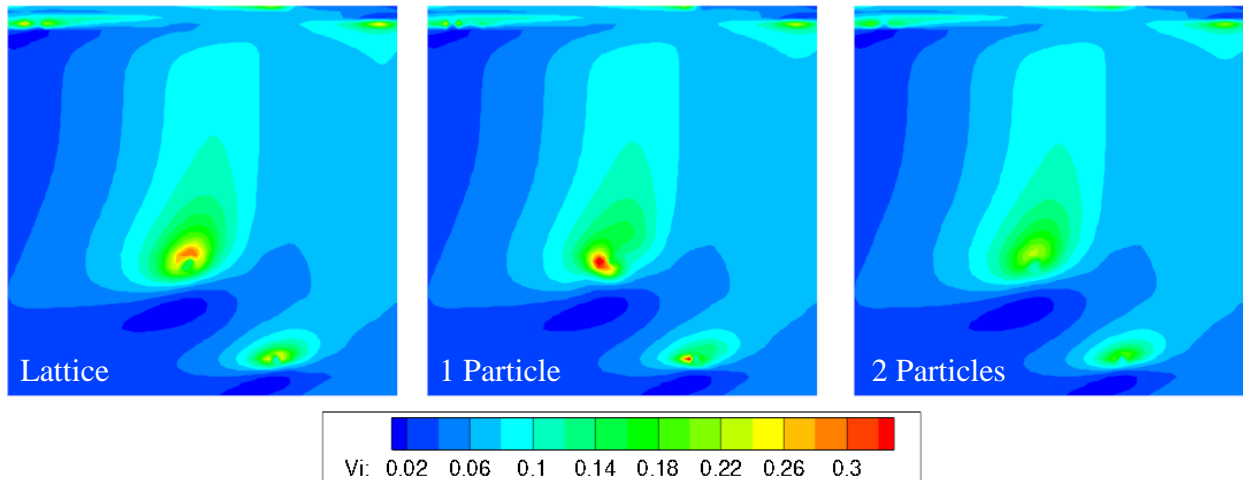
Figure 7: Wake Particle Resolution vs. Induced Velocity

It is observed that the particle wakes appear to give similar induced velocities with both 1 and 2 particles per lattice element. To quantify these results, the mean absolute percent errors are taken for both particle wakes with respect to the control. These average errors equate to 1.64% and 1.35% for the 1 and 2 particle representations, respectively. The maximum percent errors vary more; being 132% and 36% for the 1 and 2 particle wakes, respectively. However, since the averages are so close, it's safe to say that the areas affected by these larger errors is minimal. Because the errors don't decrease significantly by representing the wake with more than 1 particle per filament, the resolution from 1 particle is considered sufficient, and will be used for all following simulations due to the benefit of computational cost.

CHAPTER 3

FORWARD FLIGHT

In this chapter, the present implementation of the vortex particle methodology in GT-Hybrid is demonstrated by conducting steady forward flight simulations and comparing the results with the baseline vortex lattice wake. An extensive flight database resulting from the NASA-Army UH-60A Airloads Program [27] offers precise and repeatable experimental data to reference, including vehicle attitudes, blade airloads, structural loads, and more. Two data sources are used, one being the heavily instrumented UH-60A Airloads Aircraft [28], and the UH-60A Large Rotor Test Apparatus (LRTA), being a full-sized rotor for wind-tunnel testing in the NASA Ames 40- by 80-foot wind tunnel [29]. To capture the sectional aerodynamic lift, drag, and pitching moments, one blade on both flight and tunnel test rotors are fitted with 242 pressure transducers covering 9 radial stations, schematically shown in Figure 8:
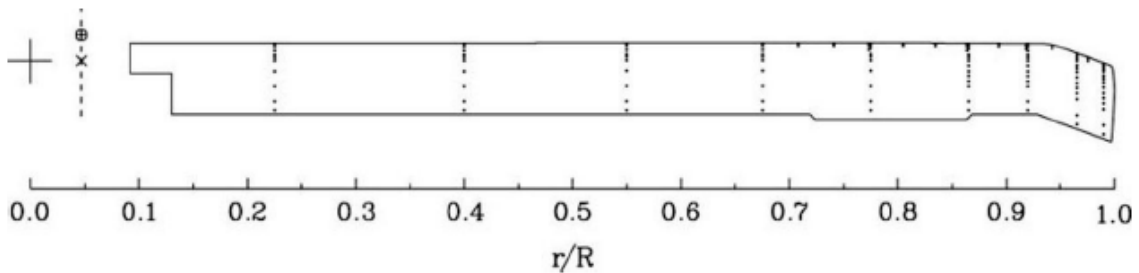
Figure 8: Pressure Transducer locations [29]

Strain gauges are also located along the blades and pitch links to get several bending moments and loads, while motion sensors are at the root to capture flapping, pitching and lead-lag angles. However, this chapter focuses on the aerodynamic loads as the ladder measurements are more critical in the following maneuvering flight section.

The specific flight conditions studied here are 8534 and 5240, resulting from the flight test and wind tunnel test, respectively. Both conditions demonstrate the UH-60A in 1-G level

flight at near maximum forward speed. Some key parameters that define them are advance ratio

(μ), blade tip Mach number ($\Omega R/a_\infty$), rotor shaft angle (α), thrust coefficient over solidity (C_T/σ),

and the hub's pitching and rolling moment (M_P & M_R), which are shown below in Table 1:

Table 1: Forward Flight Case Defining Parameters [27,29]

Case	μ	$\Omega R/a_\infty$	α	C_T/σ	M_P	M_R
C8534	0.365	0.6417	-7.31	0.084	-2583	6884
C5240	0.370	0.6417	-6.74	0.090	-2565	-2834

While these two conditions do appear very similar, there are potential effects specific to

the wind-tunnel or flight testing that could change the data in ways that cannot manipulated

within the simulations. The data provided by the wind-tunnel test is thought to be more accurate

and repeatable [29], but that does not necessarily mean that it is more representative of the actual

rotorcraft or what GT-Hybrid and DYMORE 2 are able to simulate.

Results from three simulations are shared in this chapter preceding a visualization and

discussion of the vortex lattice and particle wake convecting. The 8534 case is simulated initially

with a stand-alone vortex particle GT-Hybrid run using blade motions (trim inputs and

deformations) from a previously converged lattice wake solution. Next, 8534 is simulating via

CSD and CFD loose coupling between DYMORE 2 and GT-Hybrid with the vortex particle

method. Lastly, condition 5240 is also simulating through loose coupling. The computational

parameters used are kept consistent with the lattice wake simulations that the results are being

compared to, which have been demonstrated to be optimal for high advance ratio forward flight

[30] as studied here. These consist of grid density of 131x75x65, a time step of 0.05 degrees

azimuth, and a constant wake size of 4 revolutions. Also, particles generated at 15 equally-

spaced spanwise locations with a 5-degree azimuth wake update frequency (being when new

particles are generated, the wake is convected and boundary induced velocities are calculated).

All provided results have been obtained using a desktop Linux operating system computer with 12 processors which are model: Intel® Xenon® E5-1650 @ 3.60GHz. The computational times required using the vortex particle method are mentioned throughout and compared with that of the vortex lattice wake. Accuracy of the converged coupled simulations is then compared between the two simulations using a standardized quantifiable approach outlined in Appendix A.

3.1 Flight Test 8534

Results here are divided by the experimental data being attempted to replicate. As such, all information from this point until section 3.2 concerns the flight test 8534.

3.1.1 Wake Convection

Included in the present implementation of the vortex particle methodology in GT-Hybrid is the ability for the code to output the wake geometry and circulation strengths (contoured) at user-defined intervals. These wake files are written in formatted Tecplot® ASCII format with the iteration number at the end of their filenames. The preceding version of GT-Hybrid also does this in a similar fashion with the lattice wakes, written in formatted PLOT3D format. Shown in Figure 9 are the wakes of both methods for the initial wake (above) and wake at the end of a 2-revolution simulation (below). The lattice wakes (left) are shown with a mesh and contour, while the vortex particle wakes (right) are contoured scatter plots; thought to be representative of their underlying concepts. Videos can even be made by simply writing the wakes out at every wake time step (update frequency) which are more useful in noticing specific traits of the convection.

22
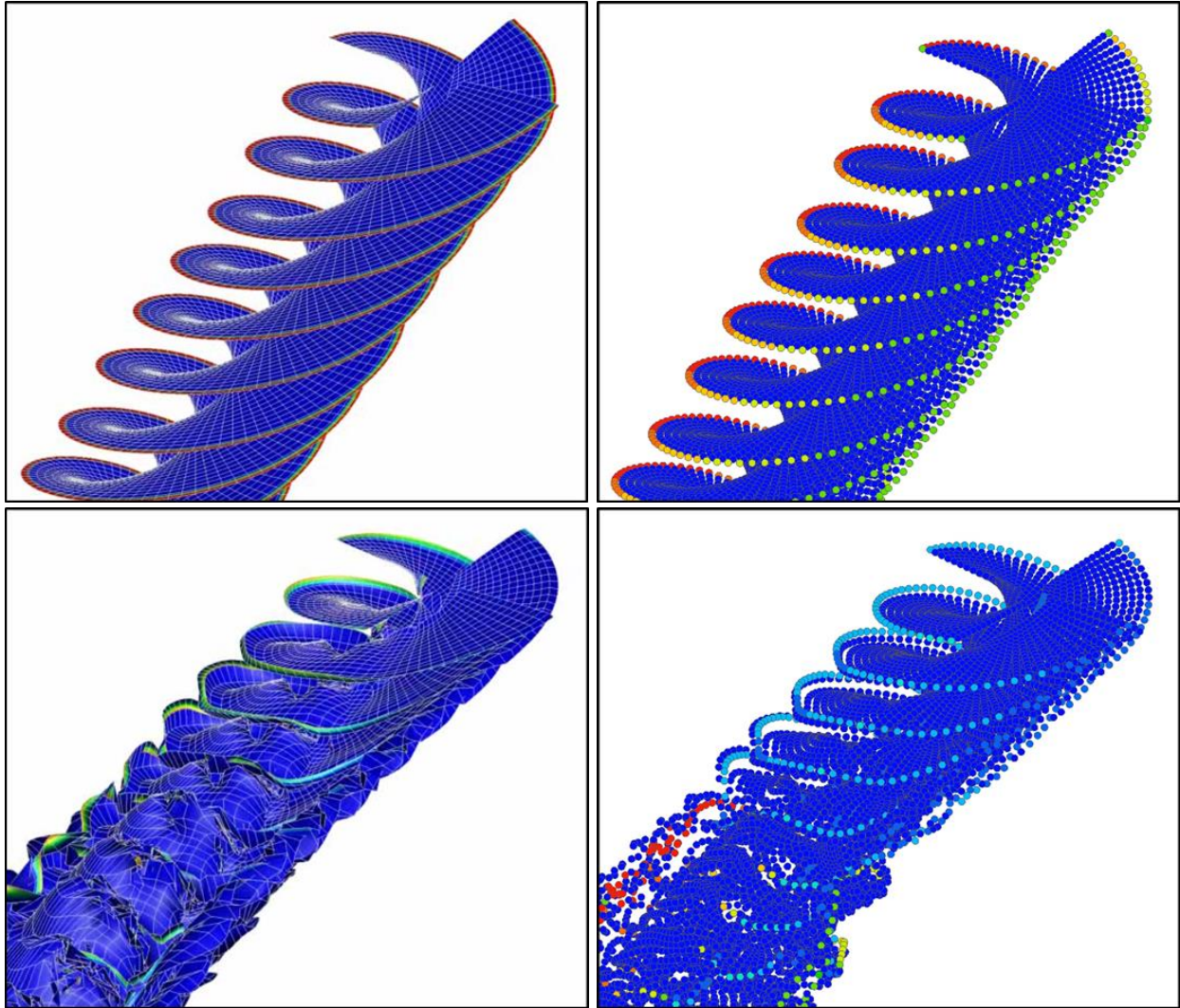
Figure 9: Forward Flight Wake Convection with Lattice (left) and Particle (right) Wakes

It is observed that the particle wake visually convects quite similarly to the lattice, sharing some significant traits. For example, both wakes stay somewhat uniformly helical until about 180-degrees from their release point and still aren't massively distorted until the vortices are about one revolution away. Since these strongly convected wake filaments exist farther away from the blade, they would have less of an effect, remembering that the induced velocity decreases with the square of the distance. This intuitively indicates that most differences in wake convection here will affect the results minimally. Notable about both wakes is that the initial helical wake shows the tip vortex strengths are much stronger than that provided by the fully

developed wakes, indicated by the contours being dominated by their lower values (blue). Furthermore, the prescribed helical wakes assume the vortices descend faster than determined by the fully developed free wake, but these descent rate still are still reasonably close throughout the simulation. A difference between the wakes is that the effect of the strong tip vortices appears more significant for the particle wake, shown by the wake "rolling up" at the edges faster than in the lattice wake. This is perhaps more obvious from seeing the videos but is consistent with the vortex particle method overpredicting induced velocities at close distances, as observed before in Figures 6 & 7 of section 2.3.4.

3.1.2 Prescribed Motions

As mentioned earlier, obtaining a converged solution for any flight case typically requires conducting about 15 CFD/CSD coupling iterations, where the blade motions found from the CSD solution become inputs to GT-Hybrid. To quickly test and compare just the GT-Hybrid results here, the blade motions of a converged solution obtained with the vortex lattice method are used in stand-alone CFD simulations, that is, no coupling is done in this section. These blade motions are used for three different variations of GT-Hybrid; first with the lattice wake, then the vortex particle wake using both the He and Zhao kernel as well as the author's kernel (described in section 2.3.2). To compare the results from the three simulations, the non-dimensional normal force (C_nM^2) and pitching moments (C_mM^2) are shown in the left and right columns, respectively, in Figure 10 below. Here these values are plotted as a function of azimuth, with $\psi=0°$ being when the blade is behind the pilot, in line with the tail boom. The vortex lattice wake's simulation is marked in the legend with "VL", then the vortex particle method using the author's and He and Zhao kernels are marked with "VP" and "VP, He and Zhao", respectively.
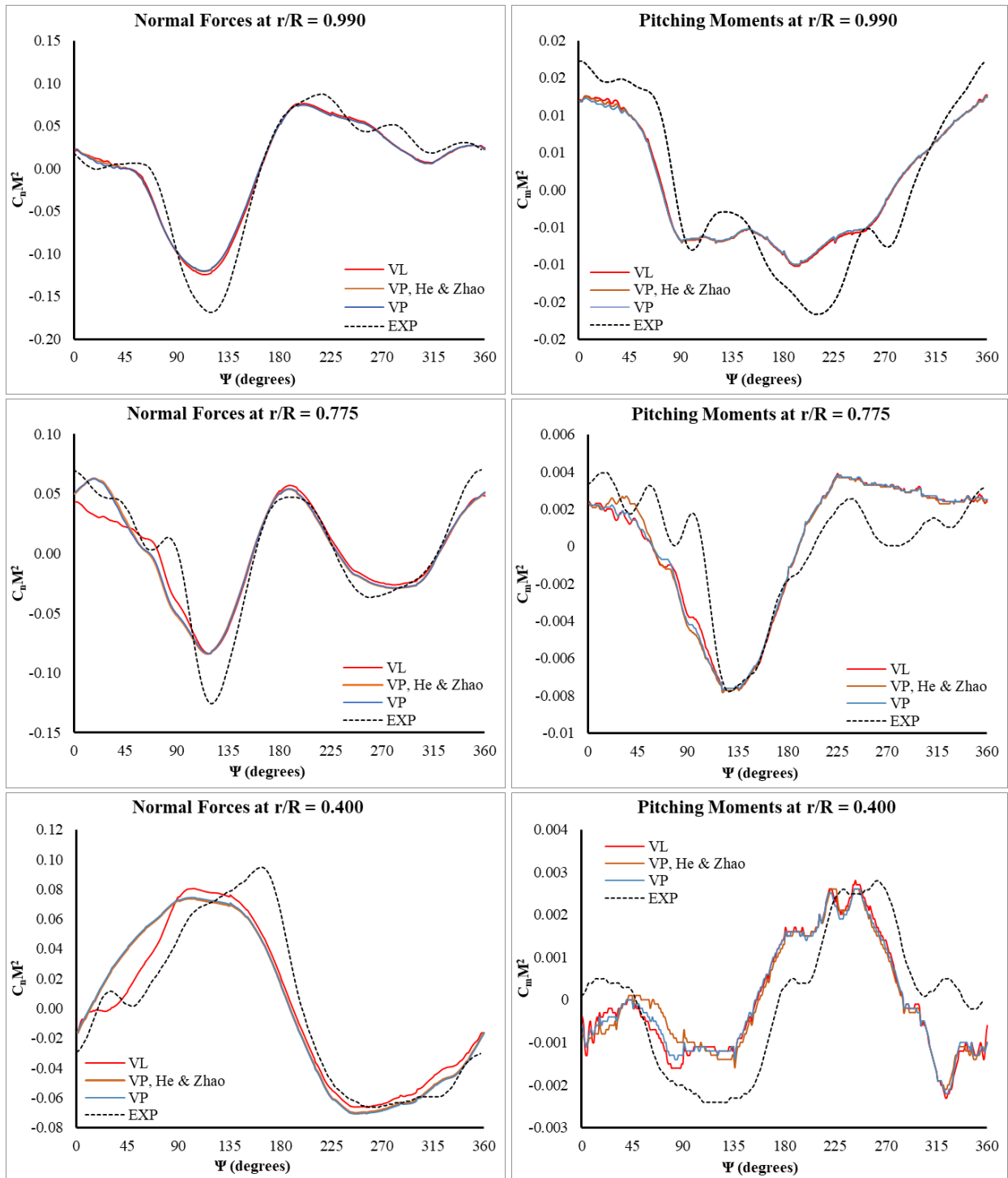
Figure 10: C8534, Prescribed Motions: Blade Sectional Airloads

It is observed that the results from the two different kernels in the vortex particle method give nearly identical results to one another, which are mostly indistinguishable except for slight differences in the pitching moments at more inboard radial stations and small azimuthal
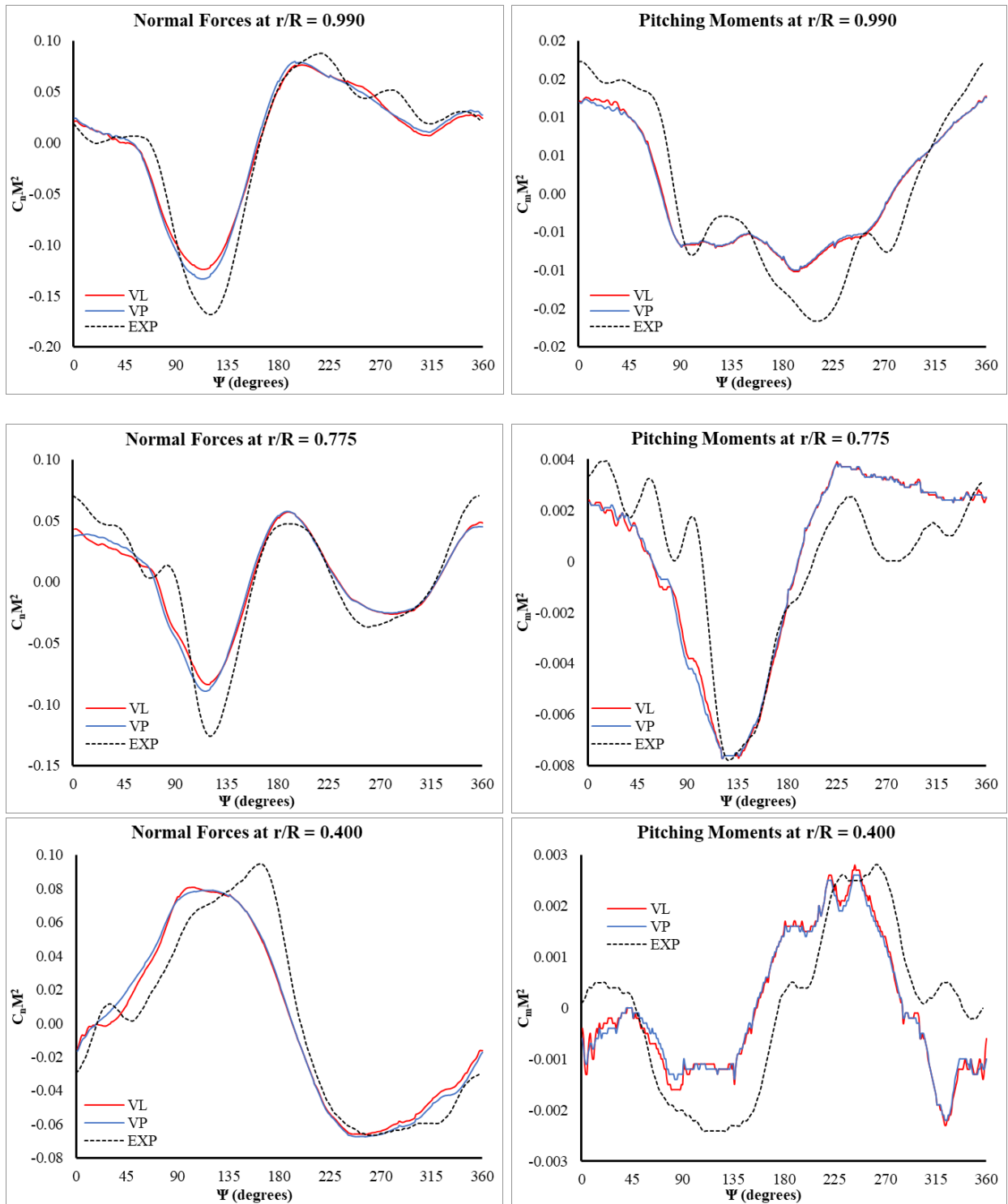
locations. The vortex particle results agree well with the lattice wake solution, with some differences in the normal loads occurring at small ψ angles, more so for the inboard radial stations. Commenting on the accuracy of the vortex particle method wouldn't be very meaningful, partly because the results are so similar but also because to capture the full effects, several CSD/CFD coupling iterations would be required. Because no coupling was done here, it was speculated that minor changes would occur. These simulations were largely conducted to get an early idea of the differences between methods and to efficiently debug and optimize the code while developing it.

More meaningful to study is the computational time, which will be looked at from two perspectives here: the time taken to complete one wake iteration, and the time for the entire solution. The wake iteration time for each method was 9.77, 10.75, and 1.35 seconds from vortex lattice, vortex particle with He and Zhao kernel, and with the author's kernel, respectively. Compared to the original vortex lattice method, this shows a 10.0% increase in wake computational time for the He and Zhao kernel, while the author's kernel gives an 86.2% decrease. Perhaps more practical to observe is how this affects the entire solution time: For the two revolutions simulated the elapsed wall-clock time was 85.37, 88.04 and 63.60 minutes for the three methods. This equates to a 3.13% increase and a 25.5% decrease in total computational time for the He and Zhao kernel and the author's kernel, respectively. Because the present implementation of the He and Zhao kernel shows no notable differences in results compared to the author's kernel and increases the computational time, it is thought to be not useful. As a result, only the author's kernel will be used to represent the vortex particle method for the following simulations.

3.1.3 Sectional Airloads, 8534

The next way to evaluate the vortex particle method is to obtain a solution by doing every CFD iteration using it, instead of just the last one as was done before. Here DYMORE and GT-Hybrid alternated for 15 loose coupling iterations per the delta-trim methodology explained in section 2.2.2, automated with a Python script. In the CFD executions: the zeroth iteration did four rotor revolutions, the first and second did three, and the rest did two. This was done for both the vortex lattice method as well as the vortex particle. Even though 15 coupling iterations took place, convergence was still confirmed by observing that the sectional loads from the 14th and 15th iterations were practically identical. Since DYMORE is now being used, structural blade and component loads were indeed calculated as a side effect. However, for 1-G level flight these are less significant than the aerodynamic forces for performance calculations and likely not something that would affect component design. Conversely, structural loads will be studied when looking at maneuvering flight in the next chapter. To avoid any discrepancies related to the zeroing of the pressure transducers and better isolate the comparisons of harmonic content and peak loads, the blade sectional loads have had their means removed. The loads here are presented in the same format as before in section 3.1.2, and are shown below in Figure 11:

Figure 11: C8534, Coupled Solution: Blade Sectional Airloads

Here the results using the vortex particle method tend to deviate from the lattice wake

solution in similar locations as seen before (Figure 10), which was expected, but the amount of

deviation did vary. On the advancing blade, a shock occurs along the outer radial stations which creates a negative pitching moment resulting in some negative lift for this region also affected by the blade vortex interaction. These are observed as valleys in the 0.775R and 0.99R normal force plots, which appear to have their magnitudes predicted slightly closer to the experimental data when using the vortex particle method. For some other results in the small azimuthal region, the loose coupling appeared to make the vortex particle solution even closer to the lattice wakes compared to the prescribed motions case. A clear example of this is looking at the normal forces at 0.4R. For several plots here, the differences between the vortex particle and lattice solutions are nearly indistinguishable, as seen for the pitching moments at 0.99R. Overall, even for the plots with more notable differences, the results are certainly very similar from a holistic point of view. The resulting accuracy will be compared quantifiably and discussed in section 3.3.

The elapsed wall-clock time required to complete the simulations shown includes both the time used on GT-Hybrid as well as DYMORE. Using the same 12-prossesor Linux machine mentioned before, obtaining the final coupled solution took 29.28 hours with the particle wake while the lattice method took 35.69 hours, equating to about a 18.0% reduction in wall-clock time by using the vortex particle method. Per iteration the times were 1.83 and 2.23 hours for the two methods, considering the 0th through 15th iteration. By checking convergence after each iteration, the total time of course has potential to decrease, but doing so hasn't been automated yet and was not done here. It is noticed that the decrease in computational time for the coupled solution (18%) is less than that for a stand-alone GT-Hybrid solution (25.5%), being due to DYMORE 2 taking about 40 minutes per iteration, a time that is of course unchanged by the selection of wake method.

3.2 Wind Tunnel Test 5240

The next forward flight case used to evaluate the wake methods GT-Hybrid is the full-scale wind tunnel test 5240. The physical parameters used as inputs to GT-Hybrid and DYMORE varied slightly from 8534 while the computational modeling parameters were the exact same (both given at the beginning of the chapter). Being that the wind tunnel testing occurred roughly two decades after the 1993 UH-60A flight testing, there are perhaps non-physical differences in the data due to changes in acquisition, along with physical differences from the testing conditions, of course.

3.2.1 Sectional Airloads, 5240

The non-dimensional blade sectional loads are shown in Figure 12 on the next page. For this simulation, the results from either wake method appear to be even closer to each other than for the previous 8534 case. Perhaps the main noticeable difference is that the vortex particle method still predicts the negative lift on the advancing blade to have a slightly larger magnitude than for the lattice wake. However, the peak-to-peak normal loads for both methods are generally overpredicted here. Conversely, the peak-to-peak pitching moments appear to be often underpredicted, particularly at the 0.4R station and 0.675R station (not shown). While the relative error of these underpredictions may be large, the absolute errors are far less significant, with the experimental peak-to-peak pitching moments at the outboard stations being as much as 5x the magnitude of that for the inboard.
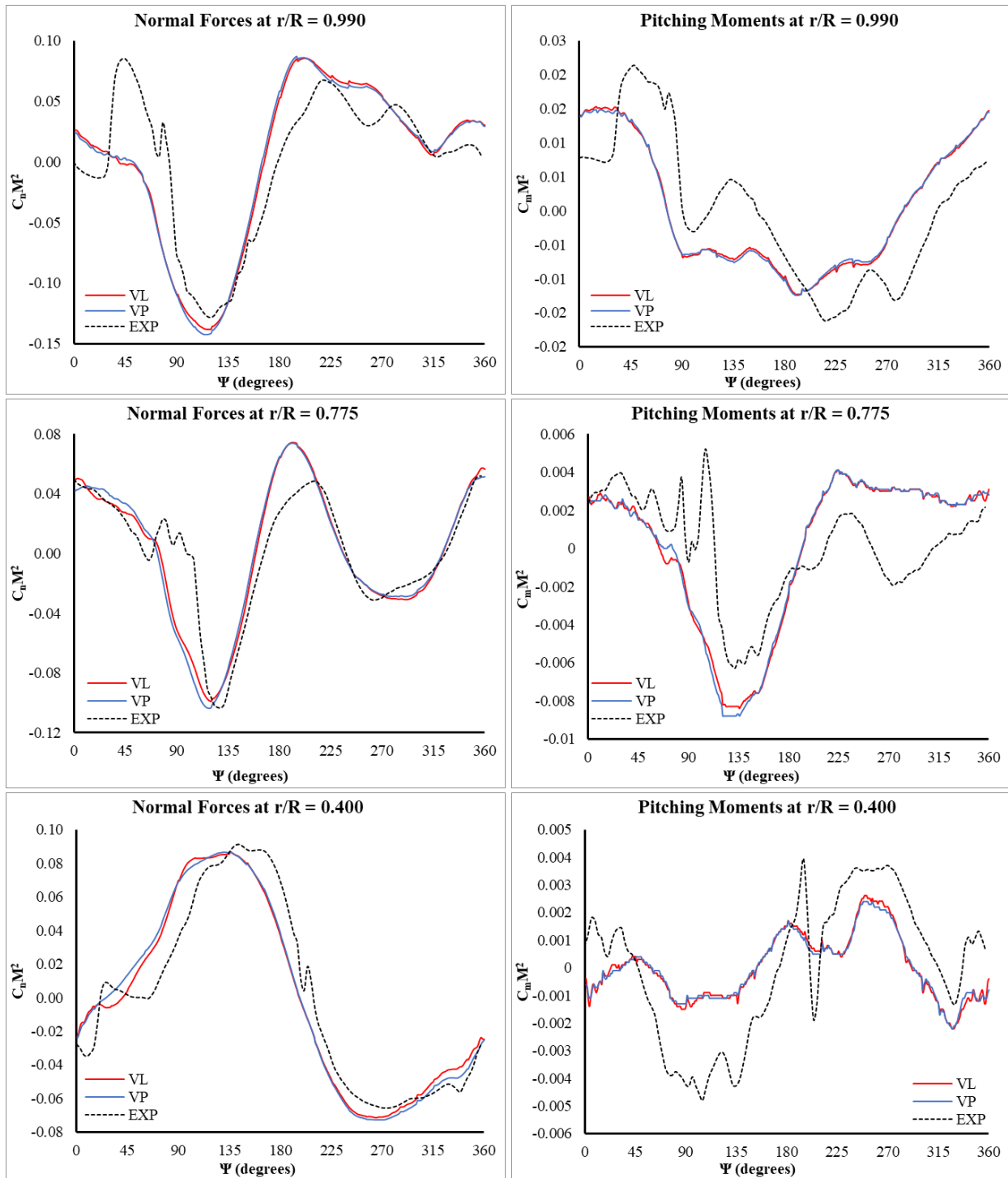
**Figure 12: C5240: Blade Sectional Airloads**

Certainly, the most significant difference when 5240 is compared to 8534 is the

experimental data. Comparing the simulation results for both tests, it is noticed that the shapes of

the waveforms look nearly identical to each other, especially for the normal loads, with some notable changes in the magnitudes occasionally. The test data, on the other hand, has effects present in the sectional loads which differ completely from test to test, many apparent in 5240 but not at all in 8534. A blatant example of this is very high lift occurring on the advancing blade just before the shock-induced negative lift occurs, seen in the normal loads and manifesting in the pitching moments as a high nose-up pitching moment. Throughout the 5240 data, very high harmonic content exists which could be just noise, which isn't seen in 8534 and is possibly due to differences in data acquisition or post processing. Either way, GT-Hybrid tends to not capture even relatively high harmonic content, making the overall correlation to 5240 appear weaker than for 8534, regardless of wake method. This will also be quantified in the next section.

Because these simulations used the same computational parameters as before, the computational cost was also the same here.

3.3 Standardized Accuracy

Here the accuracy of both 8534 and 5240 simulations is assessed with a quantitative based technique suggested by Bousman and Norman [23] and outlined in Appendix A. For these forward flight cases, only the accuracy of the blade sectional airloads is observed and is done so by gathering all normal force or pitching moment experimental data points on a single plot along with their corresponding predicted values from either the vortex particle or lattice method. This results in a point every 3 degrees azimuth for each of the 8 radial stations. Doing this for the normal loads is shown as an example in Figure 13:
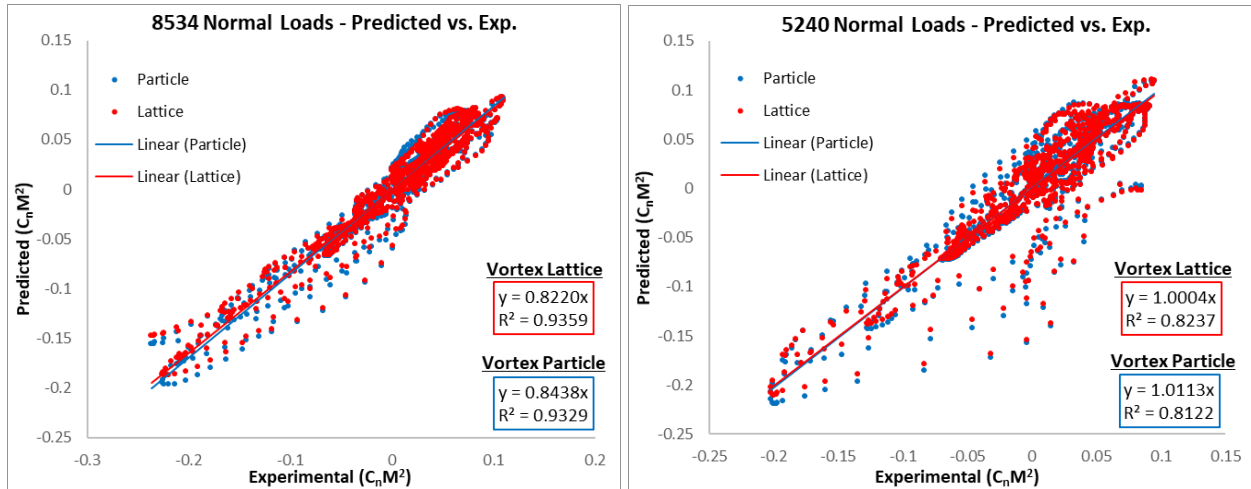
Figure 13: Predicted vs. Actual Plots for Forward Flight C_nM^2

Looking at these plots can help quantifiably confirm some trends that were mentioned earlier. For example, it had been seen the results from the particle wake simulations showed more negative lift values on the outboard advancing blade than the lattice method, which was theorized to help the 8534 normal loads correlation but hurt the 5240. This is confirmed here by observing the most negative (leftmost) values of the experimental data and the fact that the corresponding vortex particle wake predicted values reside below the lattice wake points here, increasing the resulting slope. This increase makes the slope closer to 1 in 8534, helping the correlation, but makes it farther from 1 in 5240. Another trend noticed is the amount of scatter, which is much worse in 5240. This was speculated when looking at the load plots and seeing many high frequency effects that weren't captured in the 5240 simulation and is also confirmed quantifiably by the R^2 value being much better for 8534.

Observing the predicted vs. actual plots for visual details is not guaranteed to be insightful and could just lead to more confusion. For this reason and the sake of brevity, only the resulting slope (m) and coefficient of determination (R^2) will be tabulated for comparison, as shown in Table 2 below for the two forward flight cases:

33

Table 2: Accuracy Parameters of Forward Flight Cases

Case:		8534		5240	
Wake Method:		VP	VL	VP	VL
Normal Loads	Slope	0.8438	0.8220	1.0113	1.0004
	R^2	0.9329	0.9359	0.8122	0.8237
Pitching Moments	Slope	0.6804	0.6843	0.5808	0.5805
	R^2	0.8108	0.8132	0.6911	0.6929

This concise way of analyzing the simulation accuracy shows clearly that the 8534 correlation is better than the 5240. The only instance of the 5240 being better is for the slope of the normal loads. However, considering that the slope of the linear fit could be affected by even moving one point in scatter far enough, for example, this better slope in 5240 could just be an odd coincidence. As such, the R^2 value here is seen as being more indicative of accuracy here.

CHAPTER 4

MANEUVERING FLIGHT

Helicopters in maneuvering flight demonstrate some of the most complex and unique physical phenomena known to the rotorcraft community. Non-zero translational and angular accelerations experienced by the aircraft cause highly unsteady aerodynamic loads which can occur from operating beyond the airfoil's stall region. The flexible rotor blades can experience large elastic deformations, which intensify aeroelastic effects and cause excess vibratory loads in both the rotating and non-rotating components. The large vibratory load spectrum also is a cause for concern of catastrophic fatigue failure when considering that fatigue is the most common cause of mechanical failures. Load magnitudes on control components in maneuvering flight are typically large, and it has been observed that the control loads can even be four times that experienced in high-speed forward flight [31]. As a result, loads during maneuvers typically are what govern the required strength and durability of crucial rotor and hub components. Incorrect prediction of the critical loads during an aircraft design program could lead under or oversized mechanical components, causing potentially serious issues in the future.

To analyze the efficacy of using the newly implemented vortex particle methodology in GT-Hybrid to accurately predict various loads during maneuvering flight, three extensively studied UH-60A experimental test cases are simulated. The specific maneuvers studied here all have various data on the blade aerodynamic loads, component structural loads, pilot input, etc. within the same NASA-Army UH-60A Airloads Program [9] that provided the 8534 forward flight test data in Chapter 3. However, there are of course no equivalent maneuver-replicating wind-tunnel cases here. First, two right-hand banking diving-turn maneuvers, known as 11679 and 11680, are simulated, followed by a UTTAS longitudinal pull-up maneuver. The maneuvers

are ranked by their severity by analyzing several types of structural loads. Details of each maneuver will be provided within their respective subsections.

Certain flight maneuvers are characterized as being either steady or transient depending on if there are zero or non-zero accelerations at the hub, respectively. A level turn is an example of a steady maneuver, whereas the maneuvers studied here are certainly transient. To model these maneuvers, additional velocity components are imposed on the grid rather than reorienting it. In reality, these velocities continuously vary with time by definition of being transient, however, to model them they are assumed to be piecewise constant through each distinct revolution. This application is thought to work best for slowly progressing maneuvers, where the load waveforms of the revolution being studied are close enough to that from the preceding and following revolutions. The acceleration (gravity) vector is also modified for maneuvers and the wake convects accordingly with the hub frame of reference. Using this quasi-steady approach allows for simulating a single revolution in a maneuver at a time and extending the loose-coupling methodology used in steady forward flight to maneuvers.

Significant work has been done proceeding the author's which has led to validation of using this coupled GT-Hybrid and DYMORE approach to simulate the present maneuvering flight cases. Rajmohan [9] utilized and improved aspects of this approach while validating steady level flight simulations as well as the transient UTTAS 11029 pull-up maneuver [32], [33], [34]. Marpu [13] simulated the diving turn maneuvers 11680 and 11679 [35], [36] and further refined and added to the knowledge of optimal modeling preferences.

It should be noted that the present research effort represents the first instance of using a vortex particle methodology for studying maneuvering flight. To proceed in this uncharted territory, when switching to the vortex particle method, most of the generalizations previously

36

made about GT-Hybrid's performance are thought to still hold true and thus are unchanged for this work, including factors such as the quasi-steady maneuver model, grid density, or turbulence model. This also makes the newly conducted vortex particle simulations to be a controlled study with the lattice wake simulations acting as a baseline.

4.1 Diving Turn Maneuvers

Diving turn maneuvers exhibit a rotorcraft vertically descending from high-speed forward flight as quickly as possible while doing a banking turn. These are often used in combat-related search and rescue missions, for example. During a dive turn the rotorcraft utilizes its high potential and kinetic energy to maintain very high load factor. The two UH-60A diving turns 11680 and 11679 have extensive aerodynamic and structural loads data (among other values) available in the previously mentioned flight database. Within this, 11680 is ranked as being the most severe out of all the studied maneuvers, designated by the highest push-rod loads, torsion moment at 0.3R and chord bending moment at 0.113R.

The two dive turn maneuvers here are both characterized by a right-hand bank angle (θ_b), climb rate (V_z) which is negative here for diving, average advance ratio (μ_{ave}) and a average normal load factor $(n_{z,ave})$. These values for are outlined in Table 3 below:

Table 3: Dive Turn Case Parameters [27]

Case	θ_b (deg)	V_z (ft/min)	μ_{ave}	$n_{z,ave}$
C11679	55	-3878	0.393	1.69
C11680	60	-5324	0.388	1.48

Each maneuver as recorded in the Airloads Catalog lasts about 9 seconds and 40 revolutions. Keeping these defining parameters exactly at the values in Table 3 throughout the maneuver isn't possible in a transient maneuver and isn't what's done, but the climb rate and banking angle do remain nominally constant in the severe banking portion of the maneuver. To

get a better idea of the transient nature of the maneuvers, the normal load factor is plotted against the advance ratio for each maneuver's duration in Figure 14 below:
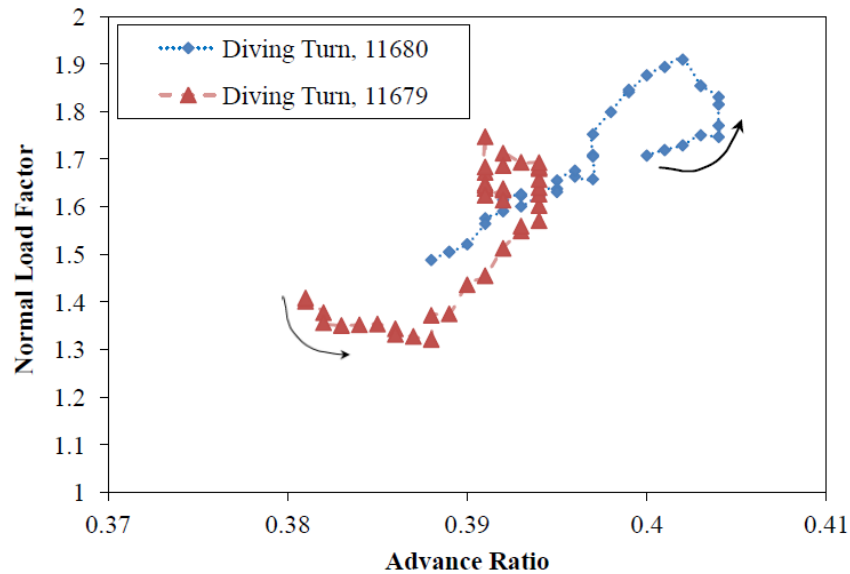
Figure 14: Advance Ratio vs. Load Factor for 11680 and 11679

The values plotted progress from the first revolution in the maneuver to the last in the direction of the arrows shown. It is seen that 11680 reaches a peak normal load factor of about 1.9, with 11679 peaking around 1.75.

Only the most severe revolutions of the maneuvers are studied here, as these are the most crucial to capture the loads for, which are then the most useful for structural design purposes. For 11680, studied is revolution 12, and revolution 20 is studied in 11679. Normal load factors near the peak values are experienced at these revolutions in the maneuvers, and some severe loads are the result of this. For example, revolution 12 of 11680 has peak-to-peak pitch link loads that are 2.5 times that experienced in high speed forward flight [37].

4.1.1 Wake Convection (Dive Turn)

Here the convecting vortex wake for a dive turn maneuver is shown, as was done for forward flight in section 3.1.1. The wake is shown in Figure 15 as its final state after two revolutions occur which convected it from the initial perfectly helical wake (not shown):
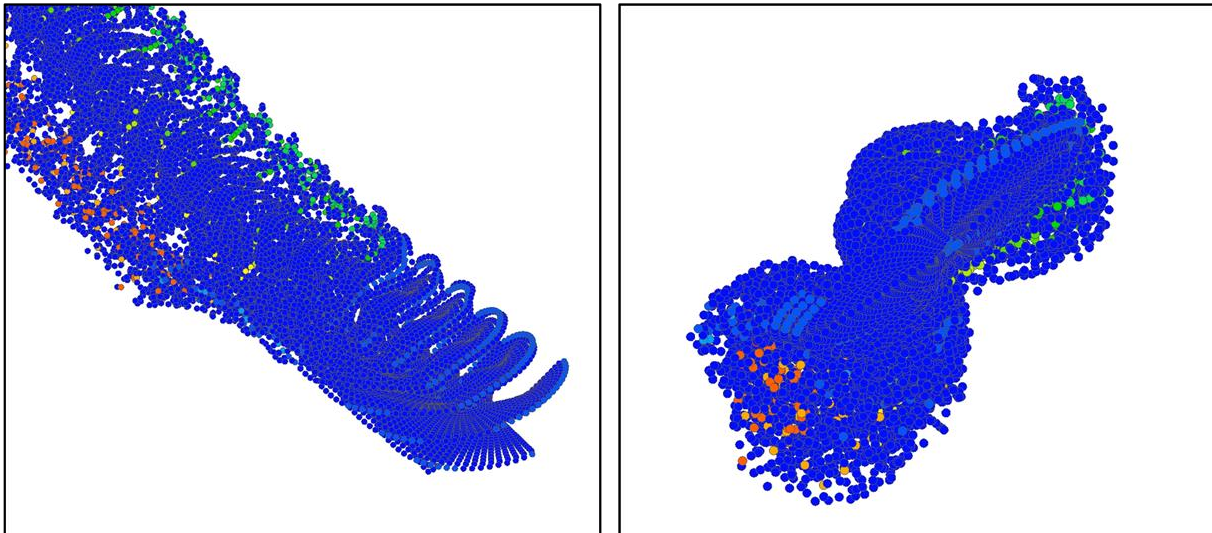
Figure 15: Dive Turn Convected Wakes with Top View (Left) and Front View (Right)

The specific wake shown is from the 11680 simulation, but the 11679 looks similar and is not shown for brevity. Only the vortex particle wake is shown also because it was observed before to convect similarly to the lattice and that holds true here as well. For the dive turn cases, the wake is seen to convect upward away from the rotor disk, which was expected given the fast, vertical descent rate of the maneuvers. This upward convection is lessoned by the rotor's downwash, which is thought to keep the wake closer to the rotor disk, thus having a greater effect on the resulting aerodynamic loads. Furthermore, from looking at the front view in Figure 15, a large vortex structure is seen to form off the advancing blades, indicating large circulation strengths in the wake. Assuming the wake does have a greater impact on the simulation than in the forward flight cases, the different wake methods used will likely vary the results more as well in these diving turn cases.

4.1.2 Sectional Airloads, 11680

The blade sectional airloads for revolution 12 of 11680 are shown in Figure 16:
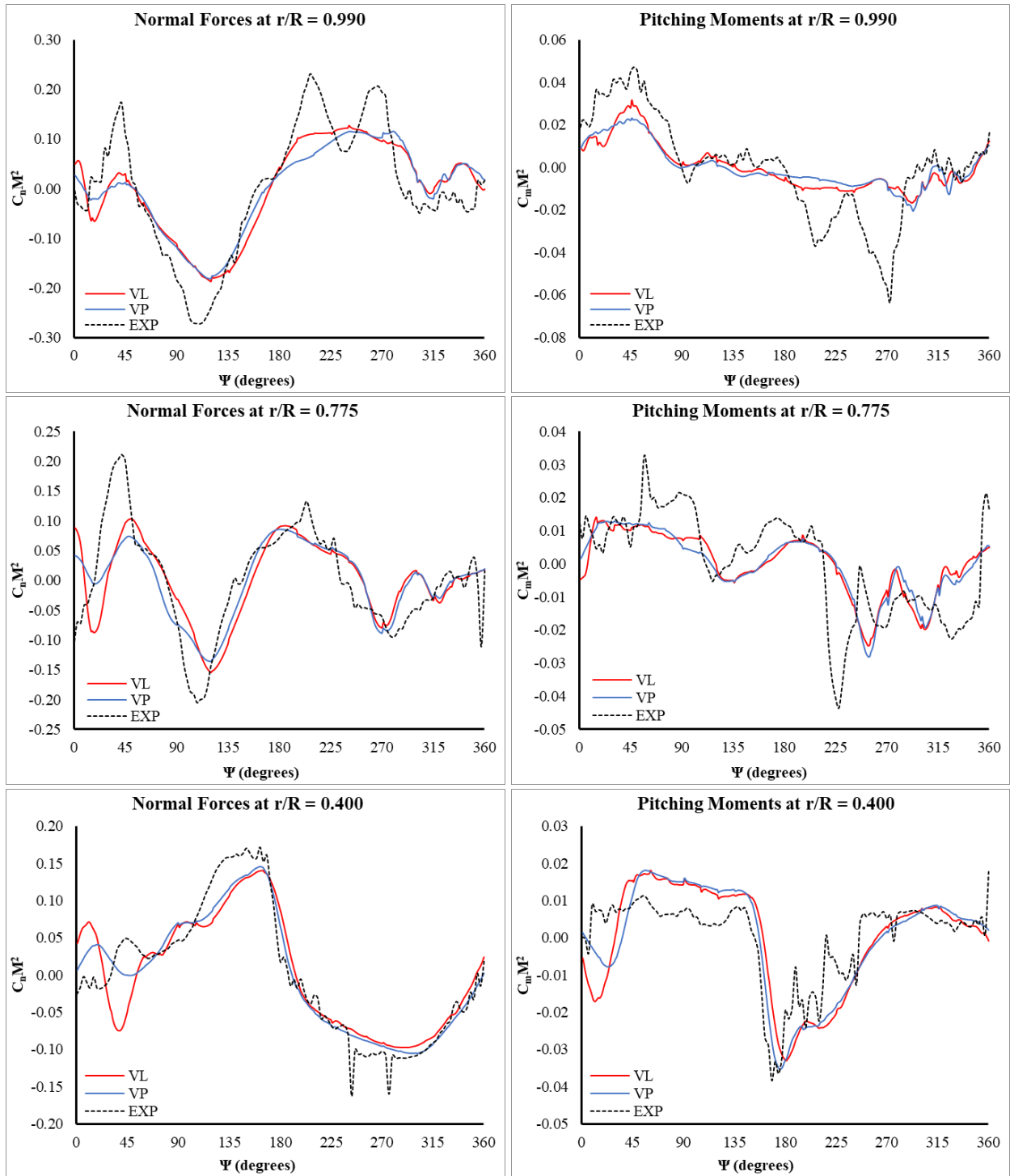

Figure 16: C11680, Rev 12: Blade Sectional Airloads

The same radial stations are shown as in the previously shared results. It is observed from these aerodynamic loads that the two wake methods do produce results that appear to vary more than in the forward flight cases, as was anticipated from viewing the wake. However, there is still no clear benefit or drawback to using either wake method that can be concluded simply by viewing these aerodynamic load plots. These plots show significant differences in waveform compared to the forward flight, and vibratory loading is observed to be more severe. Both results show that for the normal loads the 1-3P harmonics are sufficiently captured while some of the higher ones are not. This also true for the pitching moments, but even more so. Overall, the correlation looks worse than that of the forward flight cases.

4.1.3 Structural Loads, 11680

As stated earlier, strain gauges were placed on the blade at 10% radius intervals to record the flapwise bending, and less frequently for the torsional and chordwise moments. For brevity, only the 0.3R and 0.5R stations are shown for each moment type. The resulting torsional, flapwise, and chordwise moments at these stations are shown in the top, middle, and bottom row of Figure 17, respectively:
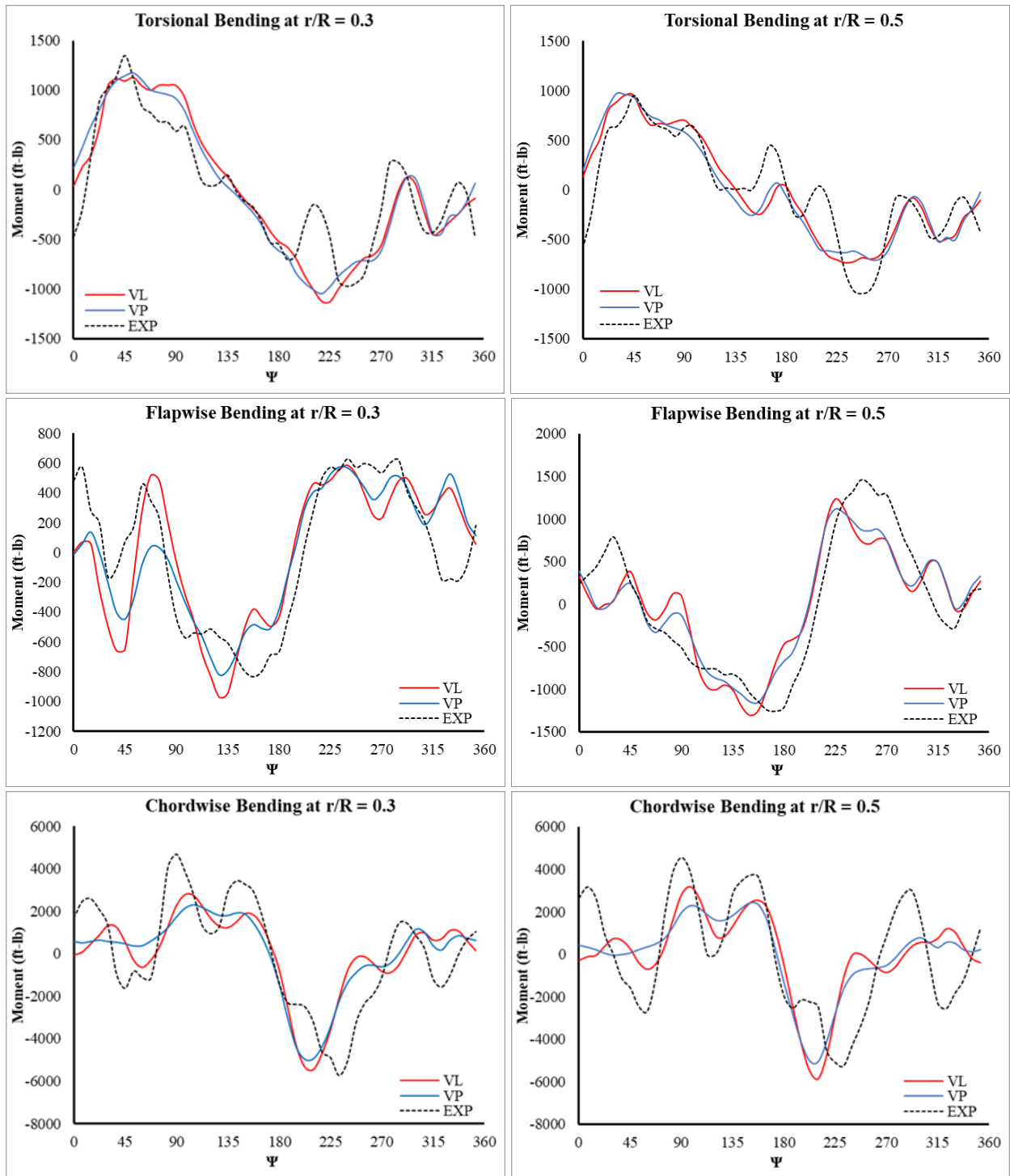
Figure 17: C11680, Rev 12: Blade Structural Loads

The structural response in the experimental data appears to have dampened out much of

the extremely high frequency that was seen in the aerodynamic loads. For the torsional and

flapwise bending, the results from both wake methods appear to correlate well with the experimental data in terms of the waveform shape and peak-to-peak, but like the previous results, higher harmonic content still generally is lacking from the simulations. It is noticed that the vortex lattice results for the flapwise and chordwise bending show the high harmonics being captured with a larger amplitude than in the vortex particle results in the first and second quadrant, while for the flapwise bending they appear to be very close. The simulations from either wake method typically underpredict the chordwise bending peak-to-peak values, and either miss some events seen in the experimental waveform or predict them significantly out of phase. This lack of accuracy in the chordwise bending can likely be attributed to the linearized damper model in DYMORE that is used here, which likely wouldn't accurately capture the inherently nonlinear force from the complex UH-60A damper, being the reason damper loads using this model are typically not correlated to the experiment. Furthermore, the damper forces affect the extent of lead-lag motion, meaning it could also affect the phase error of any simulated aerodynamic or structural forces.

The compressive/tensile forces on the pitch links during this revolution 12 of 11680 have been found to be the most severe out of any test, and the only component structural load studied here. These resulting pitch link loads are shown in Figure 18.
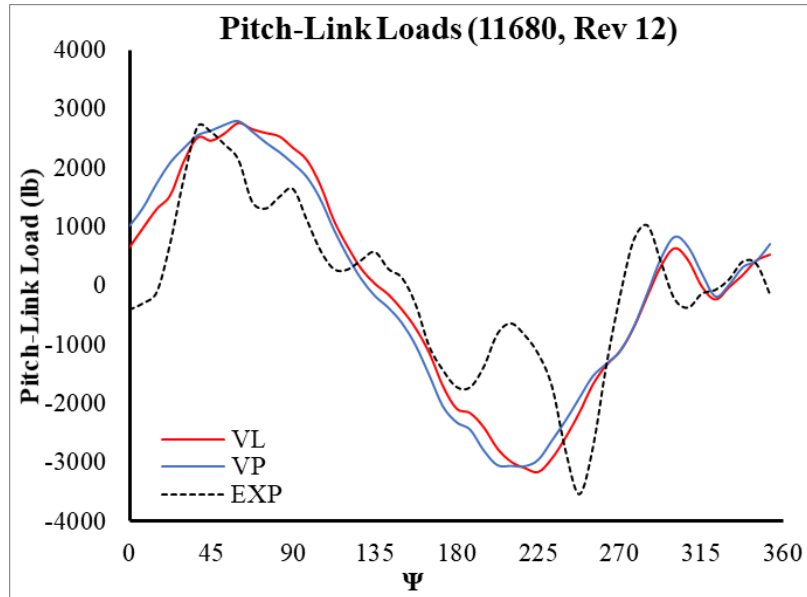
Figure 18: Pitch Link Loads (11680, Rev 12)

The simulations from either wake method appear similar but both demonstrate perhaps the most noticeable instance of the lack of capturing high frequency effects seen yet. The severity of vibratory loading has two constituents: frequency and peak-to-peak load magnitude. The one-per-rev pitch link load in the experiment is about 6240 lbs, which both wake methods capture with less than a 6% error here. As the higher frequency peak-to-peak magnitudes are much smaller, the most detrimental aspects of the pitch link loads are still considered to be captured well by the simulations, even if the high frequencies are missing. It should be noted, however, that this viewpoint of course downplays the significance of the potential vibrations imposed on other components, such as non-rotating ones, and what is felt by the rotorcraft's passengers.

4.1.4 Results from 11679

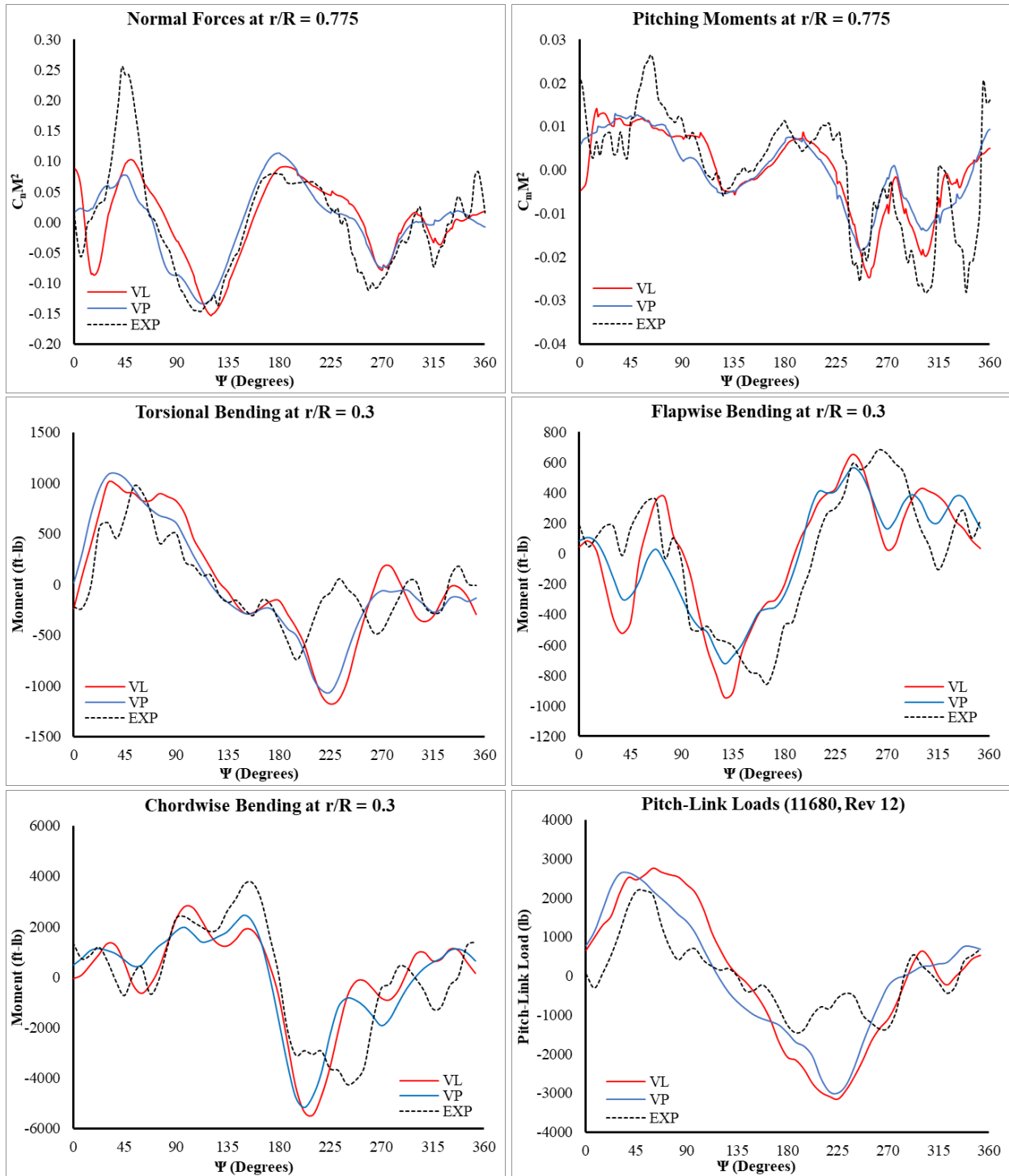Selected aerodynamic and structural loads for revolution 20 of 11679 are in Figure 19:

**Figure 19: Aerodynamic and Structural Loads from 11679, Rev 20**

For brevity, results at only one radial station per each of the six aerodynamic and structural load types are shown, which is seen as enough to explore the relatively minor differences between the two diving turn cases. One aspect is that the vortex particle wake appears to predict the phase of the normal loads better in the first and second quadrants. In the aerodynamic loads, results from either wake adequately capture two stall events in the last quadrant, which were largely missed at some radial stations in the 11680 simulations, but present in both experimental data sets. The structural blade moments show similar trends between both dive turns, although here the peak-to-peak chordwise bending is no longer underpredicted. The peak-to-peak pitch link loads are also overpredicted here by over 50%, more so for the lattice wake. However, the lattice wake solution captures the high frequency effects in the last quadrant well while the particle wake does not. The quantifiable accuracy metrics of both dive turns are at the end of the chapter.

4.2 Pull-Up Maneuver

A pull-up maneuver is defined as when a rotorcraft tilts its nose upwards sharply in forward flight to climb as quickly as possible. This kind of maneuver is practically used for obstacle avoidance, often in a military setting such as during nap-of-the-earth flight. The specific pull-up maneuver studied here is designated as flight 11029, which is based on a Utility Tactical Transport Aerial System (UTTAS) in the original UH-60A design specification [38]. Extensive data from this is again included in the UH-60 Airloads Catalog [27] which includes over 40 revolutions. In the flight database, 11029 is ranked as the second most severe condition, with the highest flapwise bending moment at 0.113R and third highest oscillatory pitch link load. 11029 begins with level flight at a high advance ratio of $\mu = 0.360$ (much like the 8534 condition), but

after a longitudinal pull-up then push-over the speed reduces to a final advance ratio of $\mu = 0.220$. This effectively draws upon the rotorcraft's high kinetic energy to increase the altitude.

Like the previous maneuvers, only the most severe revolution is studied here, which for 11029 is revolution 16. This represents about halfway into the pull-up where the speed is already reduced from 158 to 139 knots and a maximum load factor of 2.1g occurs. For several revolutions surrounding 16, the flight condition significantly exceeds the steady state McHugh lift boundary [39], where the thrust parameter peaks at $n_z C_W / \sigma = 0.165$ compared to the upper stall limit of 0.12 [40]. The $n_z C_W / \sigma$ vs. μ throughout the entire 11029 maneuver are shown in comparison to the McHugh lift boundary along with other UH-60A test conditions in Figure 20:
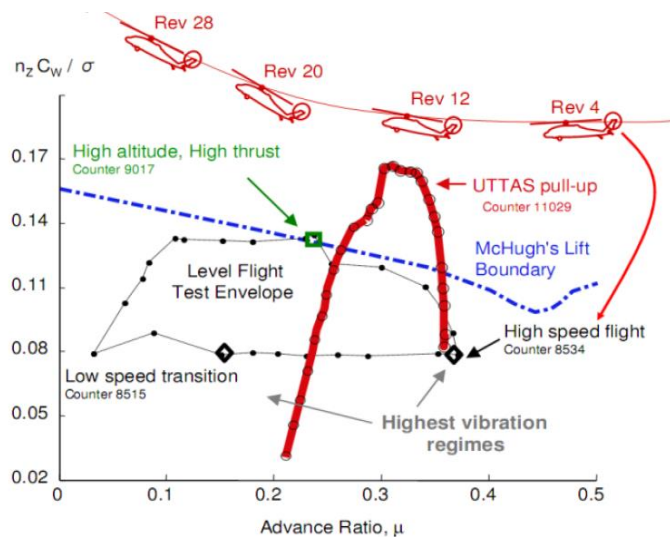
Figure 20: McHugh Lift Boundary vs. 11029 and Other Flights [39,40]

Because of this extreme condition, several stall events occur during this maneuver throughout the azimuthal range, including at outboard radial stations of the advancing blade. Furthermore, in this pull-up the wake passes through the rotor disk before being blown downstream, making simulation a challenging task. Here simulations are conducted and results from two wake methodologies are compared quantifiably. Next the vortex particle results are observed in a group comparison against another simulation using OVERFLOW/DYMORE 2.

4.2.1 Wake Convection (Pull-Up)

Like the previous simulations, the convecting wake is visualized for the 11029 UTTAS pull-up maneuver. Shown in Figure 21 is wake at near the end of a two-revolution simulation, viewed from ahead of and below the rotor.
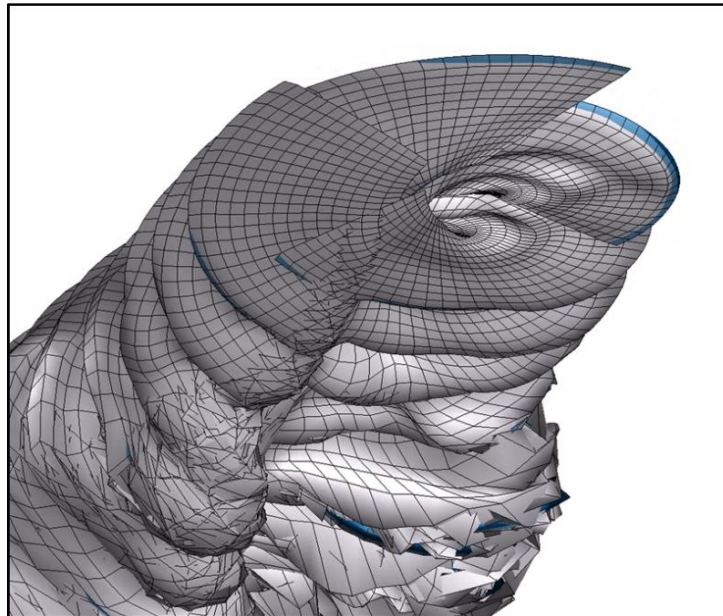
Figure 21: Wake from Pull-Up Maneuver

It should be noted that this is a vortex particle wake, even though it is shown as an un-contoured grid for viewing purposes. It is seen here that the wake convects upward in relation to the rotor disk because of the rotor tilting backwards against the fast forward freestream velocity. Large vortex structures are seen coming from both the advancing and retreating side of the rotor. The advancing blade passes through the wake of the preceding blade, occurring roughly 45 degrees azimuth. This location is also near where the advancing side dynamic stall has been observed to occur [37]. This suggests that the wake's induced velocity could contribute to changing the effective airfoil angle of attack enough to produce stall, although the true cause of the stall here is not well understood. The retreating blade also comes very close to the wake, not as clearly shown here but evident from the wake distortion in this area just after the blade.

4.2.3 Sectional Airloads, 11029

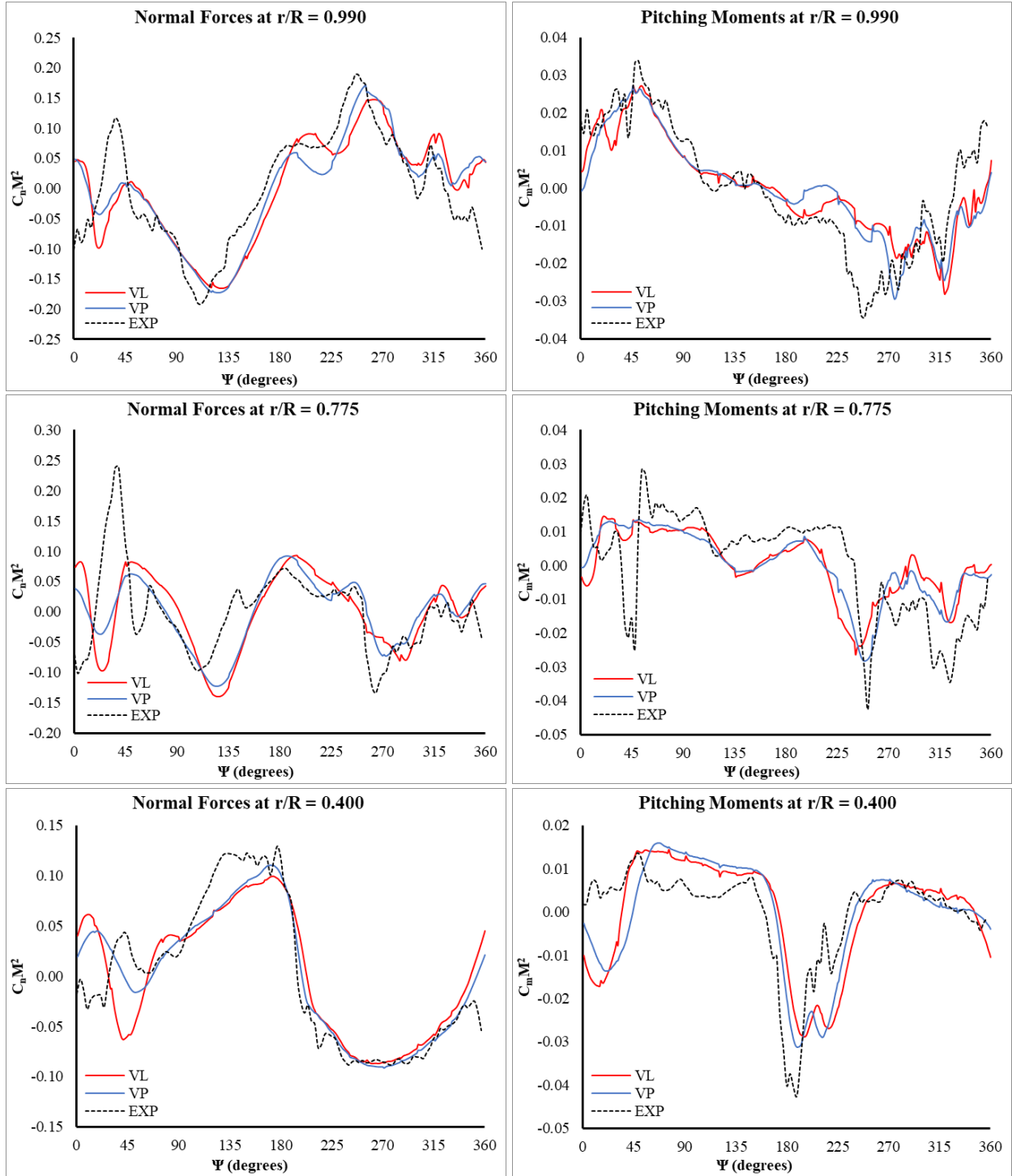The aerodynamic loads from revolution 16 of pull-up 11029 are shown in Figure 22:

Figure 22: C11029: Blade Sectional Airloads

Some of the trends observed in the aerodynamic loads of the dive turns are also observed for this pull-up, such as the lack of very high frequency effects. However, some harmonic content beyond 3P is being seen in the simulations more so than the dive turns. Here the two stall cycles on the retreating side are seen to be captured to some extent, evident in both the normal loads and pitching moments. The vortex particle method appears to be capturing these stall events better in both amplitude and phase. Stall on the advancing side is seen in the simulations, with the vortex lattice results showing it with a greater magnitude than the particle method here. However, the effects on the advancing side appear to be simulated significantly out of phase with respect to the experiment for both wake methods, so it's hard to say for certain which is doing better here. Overall, the simulations appear to be doing better here at capturing the higher harmonics, peak-to-peak, and general waveform than for the dive turns.

4.2.4 Structural Loads, 11029

Blade structural loads at 0.3R and 0.5R for revolution 16 of pull-up 11029 are shown in Figure 23 on the next page. The pitch link loads are omitted here as they are shown for the vortex particle solution in the group comparison (Section 4.2.5). For the torsional bending, the results from either wake method are quite close to each other, with the lattice results slightly leading in phase. The higher harmonics of the torsional bending are not captured adequately in the first and second quadrants and are simulated out of phase for the last two quadrants, with the vortex particle method looking better here. Looking at the flapwise and chordwise bending, the vortex particle results appear to fit the experiment much better in the first and second quadrants, especially for the inboard radial stations. Above about 225 degrees azimuth, however, the simulations are significantly out of phase, with the vortex lattice solution typically predicting the amplitudes as being larger.
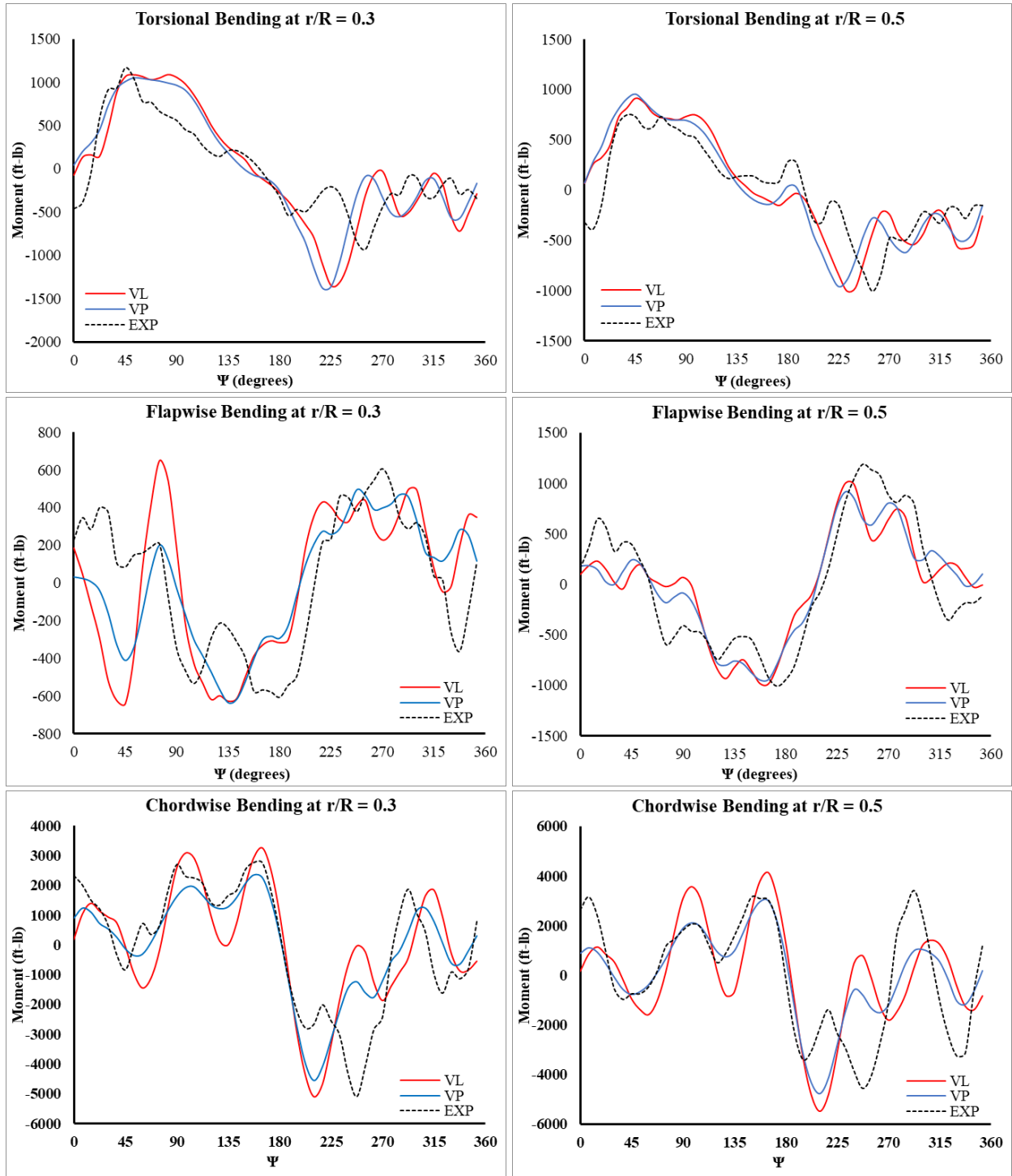
Figure 23: C11029, Rev 16: Blade Structural Loads

51

4.2.5 Group Comparison

As stated earlier, revolution 16 of the 11029 UTTAS pull-up maneuver was conducted as part of a group comparison. Here the GT-Hybrid with the vortex particle method was used by the author, while OVERFLOW was used by another group. Both members loosely coupled the respective CFD codes to DYMORE 2. Some selected loads from this are shown in Figure 24:
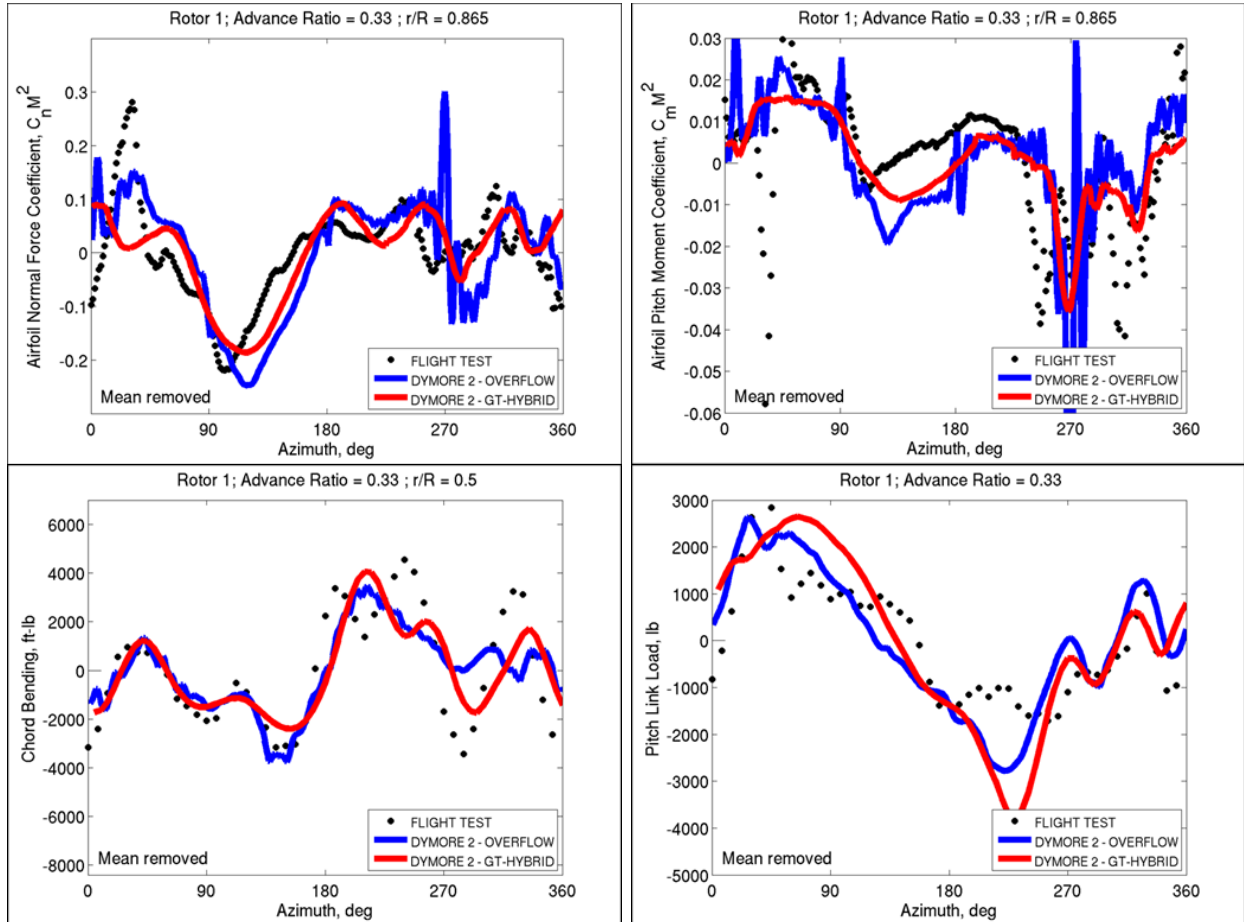
Figure 24: Group Comparison of Selected Loads from Pull-Up 11029, Rev 16

Because the OVERFLOW results aren't the author's, the correlations are compared visually here as opposed to using quantitative technique in Appendix A. The first point to mention when comparing the results from these two CFD codes is that the OVERFLOW results do have a gridded domain surrounding the entire rotor that enables fully resolving at least the near wake. This is thought to be more rigorous than GT-Hybrid's free wake model, but also

requires more computations. Considering this, however, the results from GT-Hybrid appear to correlate with the experiment competitively compared to the OVERFLOW results. In certain places on the plots shown in Figure 24, OVERFLOW clearly gives a better prediction, such as the second quadrant of the chordwise bending, and the first quadrant of the aerodynamic loads. Both solvers demonstrate the same issue in the third quadrant of the pitch link loads; showing a large fictitious valley, but GT-Hybrid appears to be doing this even worse than OVERFLOW. There are even several instances (or locations) where the GT-Hybrid solution appears to give better correlations. Most evidently, the last two quadrants of the chordwise bending have the harmonics captured better, although they are still somewhat out of phase and underpredicted. Another instance is the last quadrants of the aerodynamic loads, where GT-Hybrid doesn't show noise in the results as seen for OVERFLOW. For most of the simulation's content, it's hard to tell which code is performing better visually. The main takeaway is not that one is better than the other, but that GT-Hybrid is giving at least comparable results.

4.3 Maneuver Standardized Accuracy

Here the accuracy of each maneuver case is evaluated for the specific revolutions that were simulated. The quantitative metric for accuracy assessment (outlined in Appendix A) is again used in an equivalent way to the forward flight cases, but also applied to the structural loads here. The slopes and coefficients of determination (R^2 values) for a certain load type are contributed to by every radial station and azimuth available from the experimental data, or just every azimuth for the pitch link loads. These accuracy parameters are tabulated for either vortex lattice (VL) or vortex particle (VP) wake results in Table 4 on the next page.

Table 4: Accuracy Parameters of Maneuvering Flight Cases

Case (right):		11680 Rev 12		11679 Rev 20		11029 Rev 16	
Wake Method (right):		VP	VL	VP	VL	VP	VL
Normal Loads	Slope	0.688	0.688	0.737	0.710	0.736	0.651
	R^2	0.757	0.716	0.817	0.784	0.599	0.440
Pitching Moments	Slope	0.539	0.530	0.502	0.447	0.601	0.542
	R^2	0.459	0.471	0.467	0.371	0.502	0.443
Torsional Bending	Slope	0.890	0.903	0.924	0.914	0.971	0.976
	R^2	0.712	0.729	0.492	0.430	0.625	0.633
Flapwise Bending	Slope	0.671	0.661	0.681	0.643	0.693	0.658
	R^2	0.755	0.697	0.759	0.599	0.739	0.624
Chordwise Bending	Slope	0.470	0.456	0.585	0.548	0.571	0.509
	R^2	0.494	0.402	0.459	0.294	0.578	0.318
Pitch-Link Loads	Slope	1.104	1.113	1.376	1.366	1.145	1.120
	R^2	0.676	0.713	0.653	0.626	0.637	0.648

First looking at the results from the 11680 dive turn maneuver; most of the slopes and R^2 values are quite close to one another, with the vortex particle method generally giving values closer to unity by a few percent. Looking at the vortex lattice results as a baseline, two significant improvements are the R^2 values of the flapwise and chordwise bending, for which the vortex particle method results show an 8.32% and 22.9% improvement, respectively. To further reduce the data in Table 4, an average improvement for the slopes and R^2 is taken by using every load type in a certain maneuver. Thus, for revolution 12 of 11680, the slopes and R^2 values improved on average by 0.94% and 4.48%, respectively. Although some accuracy parameters were much better using the vortex particle wake, since some were roughly the same and some worse, so the average improvements here are not huge, but improvements nonetheless.

Moving on to the 11679 dive turn; every accuracy parameter is improved by using the vortex particle method, with one exception being the pitch link loads' slope (worse by only

0.73%). Many of these differences are quite significant: for example, the aerodynamic pitching moment's slope improved by 12.3% and R^2 by 25.9%. Additionally, the R^2 values for the flapwise bending moment improved by 26.7%, and for the chordwise bending 56.1%. Again, taking averages of all the loads differences for the 11679 case; the vortex particle method showed an average improvement of 4.86% and 21.9% for the slope and coefficient of determination, respectively.

Lastly, the results from the 11029 pull-up maneuver: a minute drawback is seen in the torsional moments and consequently the pitch link loads, but the maximum decrease is only about 2%. Apart from this, every other accuracy parameter is improved from using the vortex particle method, and most show an even larger improvement than seen in the dive turn maneuvers. For example, the slope and R^2 value for the aerodynamic normal loads increased by 13.1% and 36.1%, respectively. Furthermore, the R^2 for the flapwise bending improved by 18.8% and the chordwise by 81.8%. For the 11029 pull-up overall, average improvements for the slope and R^2 are 6.45% and 24.4%, respectively.

Some generalizations can be made by looking at the accuracy parameters of each maneuver side by side. Comparing the 11679 results from either wake method to the 11680 results, the pitching related loads (aerodynamic pitching, torsion and pitch link) typically have slightly worse accuracy parameters but all others are better. As such, the overall correlations from either dive-turn simulation are said to be similar. For the 11029 pull-up, the correlation (with either wake) is stronger than for either dive turn maneuver, evident by nearly every accuracy parameter. Generalizing for every maneuver, the pitch link loads from the vortex particle method are slightly worse, and sometimes the blade torsion as well. Most loads, however, have consistently improved or similar accuracy parameters.

CHAPTER 5

CONCLUSIONS AND RECOMMENDATIONS

The present research expands the understanding of the vortex particle method and its behavior when applied to rotorcraft aerodynamics in a variety of flight conditions for the UH-60A rotor. Initially, studies were conducted to investigate traits of two specific techniques (kernels) to calculate the induced velocity of a wake constructed with a field of independent points with vector-valued vorticities. The vortex particle method and vortex lattice method, where vorticity vectors are connected tip-to-tail in a lattice fashion, were also compared in some preliminary small-scale problems to help identify differences in the models.

The hybrid Navier-Stokes/free wake model CFD code, GT-Hybrid, was supplemented with the vortex particle wake methodology in place of the existing lattice wake. Results from the two wake models were compared by performing simulations using GT-Hybrid loosely CFD/CSD coupled to a multi-body dynamics rotorcraft comprehensive code, DYMORE 2. Several flight conditions were studied with available experimental data recorded in the UH-60A flight test database. This includes high-speed steady level flight and transient diving turn and pull-up maneuvers, modeled with a quasi-steady loosely coupled approach. This research demonstrates the first instance of the vortex particle methodology being applied to maneuvering flight.

Ultimately, the intent of this work is to validate GT-Hybrid with its addition of a vortex particle method and generalize aspects of its performance. Users of GT-Hybrid can gain an understanding of some key differences compared to the lattice wake method, and also have an idea of the level of confidence that can be had when using the vortex particle method in future applications.

5.1 Concluding Remarks

Based on the studies performed in this work, the following conclusions may be drawn:

1. The methodology of loosely coupling a hybrid wake rotorcraft CFD code to a comprehensive multi-body dynamics code, via GT-Hybrid and DYMORE 2, provides a computationally efficient way to simulate level and maneuvering flight that can even be done with a desktop computer.

2. Supplementing GT-Hybrid with a vortex particle wake method can significantly benefit the efficiency by reducing the wake's computational time by a nearly a factor of 8, here resulting in a roughly 25% time decrease for a stand-alone CFD solution, or 19% decrease with loose coupling.

3. The forward flight cases had the best overall correlations using either wake method, followed by the pull-up maneuver, then dive turn maneuvers.

4. The correlations for most load types in every maneuvering flight case were improved by using the vortex particle wake when compared to the lattice wake results, indicated by the linear regression curve-fit accuracy assessment.

5. For the high-speed forward flight cases, relatively minor differences were seen in the prediction accuracy of GT-Hybrid by using either wake methodology.

6. The magnitudes of the higher harmonic content tend to be predicted as smaller when using the vortex particle wake, sometimes helping the correlation and sometimes hurting it, but a distinct factor to consider either way.

7. The aerodynamic normal loads and chordwise and flapwise bending predictions were consistently and significantly improved by the vortex particle method, while the pitching related loads were often either similar or slightly worse.

5.2 Recommendations for Future Work

While the present research has strengthened the understanding of many aspects and details of the vortex particle wake methodology, much more work could be done to further the knowledge of its application. There is also of course potential for improvement in other areas of GT-Hybrid that could help its prediction accuracy or computational cost. As such, the following recommendations are offered for future research:

1. The general waveform of loads is generally well captured, but accurately predicting both phase and magnitude of higher harmonic content could be improved upon.

2. To precisely locate any accuracy drawbacks associated with the hybrid wake approach, comparisons of results from a CFD code that fully resolves the wake could be done.

3. The amount of vortex filaments used to represent a wake has been studied in the past and moderately here, but more work should be done to better generalize the effects of vortex particle resolution on the resulting prediction accuracy.

4. Understanding of the prediction accuracy of GT-Hybrid with the vortex particle method could be enhanced by simulating other flight conditions or even other rotors.

5. Parallel processing the vortex particle calculations may further help computational time.

6. To further improve the time required with CFD/CSD coupling, implementing the vortex particle methodology into DYMORE's aerodynamic model could be advantageous.

APPENDIX A

QUANTITATIVE ACCURACY ASSESMENT

Determining the overall accuracy of a simulation with respect to experimental data is not a straightforward task, but certainly an important one. With more variables present, it becomes more and more difficult to generalize about the correlations. Coming to conclusions by visual analysis, for example using line plots for the different load types, can be misleading or subjective to the viewer. To avoid human error in visual analysis, a standardized approach for quantitative assessment of the predictive accuracy of rotorcraft aeromechanics tools was proposed by Bousman and Norman [23].

The procedure consists of plotting experimental values for a certain parameter on the x-axis with corresponding predicted values on the y-axis. If the predictions match the experiment perfectly this would produce a line with a slope of 1.0 and y-intercept of 0.0. In actuality, a scatterplot is formed, for which a linear regression curve-fit is done and provides up to three attributes of correlation quality; a slope (m), coefficient of determination (R^2) and vertical offset (b). A correlation is then said to be better if its slope and coefficient of determination are closer to one and the y-intercept is closer to zero. The accuracy parameters (m, R^2 or b) can also indicate certain trends about the correlation. For example, a difference in the y-intercept is indicative of an error in the mean value prediction, so removing the means (as done here) effectively eliminates b. Also, slopes larger than 1.0 are considered overpredictions and less than 1.0 being underpredictions. The R^2 value varies with the amount of scatter, which can result from results being out of phase or local magnitude errors, potentially making it the most significant parameter in assessing the accuracy of the prediction.

REFERENCES

[1]   Ahmad J., Duque, E. P. N., and Strawn, R. C., "Computations of Rotorcraft Aeroacoustics with a Navier-Stokes/Kirchhoff Method," 22nd European Rotorcraft Forum, Brighton, UK, Sept. 17-19, 1996.

[2]   Bauchau, O. A. and Ahmad, J. U., "Advanced CFD and CSD Methods for Multidisciplinary Applications in Rotorcraft Problems", Proceedings of the AIAA/NASA/USAF Multidisciplinary Analysis and Optimization Symposium, Bellevue, WA, Sep. 4-6, 1996, pp.945-953.

[3]   Chaderjian, N. and Ahmad, J. "Advancing Rotorcraft Simulation Using Computational Fluid Dynamics," *NASA Ames Research Center,* 2015. https://www.nas.nasa.gov/SC13/demos/demo4.html

[4]   Sankar, L. N., Bharadwaj, B. K., and Tsung, F. L., "A three-dimensional Navier-Stokes/full-potential coupled analysis for viscous transonic flow," AIAA 10th Computational Fluid Dynamics Conference, Honolulu, HI, June 24-27, 1991.

[5]   Berezin, C. R. and Sankar, L. N., "An Improved Navier-Stokes/Full Potential Coupled Analysis for Rotors," Mathematical Computational Modeling, Vol.19, No.3/4, 1994, pp.125-133.

[6]   Yang, Z., Sankar, L. N., Smith, M. J., and Bauchau, O., "Recent Improvements to a Hybrid Method for Rotors in Forward Flight," Journal of Aircraft, Vol. 39, No. 5, 2002, pp. 804-812.

[7]   Van Leer, B. "Towards the ultimate conservative difference scheme. V. A second-order sequel to Godunov's method," Journal of computational Physics Vol. 32, No. 1, 1979, pp. 101-136. http://dx.doi.org/10.1016/0021-9991(79)90145-1

[8]   Yoon, S., and Jameson, A. "Lower-upper Symmetric-Gauss-Seidel method for the Euler and Navier-   Stokes equations," AIAA Journal Vol. 26, No. 9, 1988, pp. 1025-1026. DOI: 10.2514/3.10007

[9]   Rajmohan, N. "Application of Hybrid Methodology to Rotor in Steady and Maneuvering Flight," School of Aerospace Engineering. Georgia Institute of Technology, Atlanta, GA, 2010.

[10]   Spalart, P. R. and Allmaras, S. R., "A One-Equation Turbulence Model for Aerodynamic Flows," La Recherche Aerospatiale, 1994.

[11]   Rajmohan, N., Egolf, T. A., Flemming, R. "GT-Hybrid User Manual and Theory Overview Version 3.34," *School of Aerospace Engineering.* Georgia Institute of Technology. Atlanta, GA, 2010.

[12]   Collins, K. "A Multi-Fidelity Framework for Physics Based Rotor Blade Simulation and Optimization," *School of Aerospace Engineering.* Georgia Institute of Technology. Atlanta, GA, 2008.

[13]   Marpu, R. "Physics Based Prediction of Aeromechanical Loads for UH-60A Rotor," *School of Aerospace Engineering.* Georgia Institute of Technology, Atlanta, GA, 2013.

[14] Kuethe, A., and Chow, C.-Y. Foundations of Aerodynamics: New York: John Wiley and Sons Inc, 1998.

[15] Mello, O. A. F., Prasad, J. V. R., Sankar, L. N., and Tseng, W., "Analysis of Helicopter/Ship Aerodynamic Interactions", American Helicopter Society Aerodynamics Specialists Conference, San Francisco, California, Jan. 19-21, 1994.

[16] Leishman, J., Bagai, A. "Challenges in Understanding the Vortex Dynamics of Helicopter Rotor Wakes," *AIAA Journal* Vol. 36, No. 7, 1998, pp. 1130-1140. https://doi.org/10.2514/2.510

[17] Vatistas, H., Kozel, V., Mih, W. "A Simpler Model for Concentrated Vortices." Experiments in Fluids Vol. 11, No. 1, 1991, pp. 73-76. DOI: 10.1007/BF00198434

[18] Bhagwat, M., Leishmanm G. "Generalized Viscous Vortex Model for Application to Free-Vortex Wake and Acoustic Calculations," *Annual Forum Proceedings-American Helicopter Society.* Vol. 58, American Helicopter Society, Inc., 2002, pp. 2042-2057.

[19] Bauchau, O. A. "Computational Schemes for Flexible, Nonlinear Multi-Body Systems," *Multibody System Dynamics* Vol. 2, No 2. 1998, pp. 169-225. DOI: 10.1016/S0895-7177(00)00303-4

[20] Johnson, W. "Rotorcraft dynamics models for a comprehensive analysis," Annual Forum Proceedings-American Helicopter Society, Vol. 54, American Helicopter Society, 1998, pp. 452-471.

[21] Saberi, H., Khoshlahjeh, M., Ormiston, R. A., and Rutkowski, M. J. "Overview of RCAS and application to advanced rotorcraft problems," American Helicopter Society 4th Decennial Specialists' Conference on Aeromechanics, San Francisco, CA. 2004.

[22] Abhishek, A., Datta, A., and Chopra, I. "Prediction of UH-60A structural loads using multibody analysis and swashplate dynamics," Journal of Aircraft Vol. 46, No. 2, 2009, p. 474. doi: 10.2514/1.35076

[23] Bousman, W. G., Norman, T. "Rotorcraft Airloads Measurements: Extraordinary Costs, Extraordinary Benefits," *Journal of the American Helicopter Society*. Vol. 59, 2014. DOI: 10.4050/JAHS.59.031001

[24] Phanse, S., Sankar, L. N., Charles, B. D., "Efficient Coupled Fluid Structure Interaction Approach for Analysis of Rotors in Forward Flight," *American Helicopter Vertical Lift Aircraft Design Conference*, San Francisco, California, January 18-29,2006

[25] Altmikus, A., Wagner, S., Beaumier, P., and Servera, G. "A comparison- Weak versus strong modular coupling for trimmed aeroelastic rotor simulations," AHS International, 58th Annual Forum Proceedings. Vol. 1, 2002, pp. 697-710.

[26]   Tung, C., Caradonna, F. X., and Johnson, W. R. "The prediction of transonic flows on an advancing rotor," Journal of the American Helicopter Society Vol. 31, No. 3, 1986, pp. 4 -9. http://dx.doi.org/10.4050/JAHS.31.4

[27]   He, C. and Zhao, J. "Modeling Rotor Wake Dynamics with Viscous Vortex Particle Method," *AIAA Journal* Vol. 47, No. 4, 2009, pp. 902-915.

[28]   Leonard, A. "Computing Three Dimensional Incompressible Flows with Vortex Elements," *Annual Review of Fluid Mechanics* Vol. 17, 1985, pp. 523-559. https://doi.org/10.1146/annurev.fl.17.010185.002515

[27]   Bousman, W. and Kufeld, R. "UH-60A Airloads Catalog," *Aeroflightdynamics Directorate (AMRDEC) U.S. Army Research, Development, and Engineering Command.* Ames Research Center. Moffett Field, California, 2005. NASA/TM-2005-212827, AFDD/TR-05-003

[28]   Kufeld, R., Dwight, L., Balough, D., Cross, J., Studebaker, K., Jennison, C., Bousman, W. "Flight Testing the UH-60A Airloads Aircraft," *Proceedings of the 50th Annual Forum of the American Helicopter Society.* Washington, DC, 1994.

[29]   Norman, T., Shinoda, P., Peterson, R., Datta, A. "Full-Scale Wind Tunnel Test of the UH-60A Airloads Rotor," *Annual Forum Proceedings-American Helicopter Society,* Vol. 67, American Helicopter Society, Inc., Virginia Beach, VA, 2011, pp. 3-5.

[30]   Marpu, R., Sankar, L., Norman, T., Egolf, T., Makinen, S. "Analysis of the UH-60A Rotor Loads Using Wind Tunnel Data," *51st AIAA Aerospace Sciences Meeting including the New Horizons Forum and Aerospace Exposition.* Grapevine, TX, 2013.

[31]   Kufeld, R, Bousman, W. "High Load Conditions Measured on a UH-60A in Maneuvering Flight," *Journal of the American Helicopter Society* Vol. 43, No. 3, 1998, pp. 202-211. http://dx.doi.org/10.4050/JAHS.43.202

[32]   Rajmohan, N., Sankar, L., Costello, M. "Effect of Inflow Modeling on Coupling between Rotor Flight Mechanics and Aeromechanics," *49th AIAA Aerospace Sciences Meeting including the New Horizons Forum and Aerospace Exposition*. Orlando, FL, 2011.

[33]   Rajmohan, N., Manivannan, V., Sankar, L., Costello, M., Bauchau, Olivier. "Development of a Methodology for Coupling Rotorcraft Aeromechanics and Vehicle Dynamics to Study Helicopters in Maneuvering Flight," *Annual Forum Proceedings-American Helicopter Society.* Vol. 65, American Helicopter Society, Inc., 2009.

[34]   Rajmohan, N., Marpu, R., Sankar, L. N., Baeder, J. D., and Egolf, T. A. "Improved prediction of rotor maneuvering loads using a hybrid methodology," Annual Forum Proceedings-American Helicopter Society. Vol. 67, 2011.

[35]   Marpu, R., Sankar, L. N., Makinen, S., Baeder, J. D., Egolf, T. A., and Wasikowski, M. "Physics based modeling of maneuver loads for rotor and hub design," *American*

Helicopter Society Specialist's Design Conference. American Helicopter Society, Inc., San Fransisco, 2012.

[36]   Marpu, R., Sankar, L. N., Makinen, S., and Baeder, J. D. "Computational Modeling of Diving-Turn Maneuvers using Hybrid Methodology," Annual Forum Proceedings American Helicopter Society. Vol. 68, American Helicopter Society, Inc., Fort Worth, TX, 2012.

[37]   Bousman, W. G. "A qualitative examination of dynamic stall from flight test data," Journal of the American Helicopter Society, Vol. 43, No. 4, 1998, pp. 279-295. http://dx.doi.org/10.4050/JAHS.43.279

[38]   Abhishek, A., Ananthan, S., Baeder, J., and Chopra, I. "Prediction and Fundamental Understanding of Stall Loads in UH-60A Pull-Up Maneuver," Journal of the American Helicopter Society, Vol. 56, No. 4, 2011. http://dx.doi.org/10.4050/JAHS.56.042005

[39]   McHugh, F. J., "What Are the Lift and Propulsive Force Limits at High Speed for the Conventional Rotor?" American Helicopter Society 34th Annual Forum Proceedings, Washington, DC, May 15-19, 1978.

[40]   Bhagwat, M. J., Ormiston, R. A. ,Saberi, H. A. and Hong, X., "Application of CFD/CSD Coupling for Analysis of Rotorcraft Airloads and Blade Loads in Maneuvering Flight," American Helicopter Society 63rd Annual Forum, Virginia Beach, VA, 2007